

# **Tropical Cyclone Diurnal Cycle Signals in a Hurricane Nature Run Simulation**

Jason P. Dunion<sup>1</sup> and Christopher D. Thorncroft<sup>2</sup>

1 University of Miami/CIMAS - NOAA/AOML/Hurricane Research Division, Miami, FL

2 University at Albany/SUNY

Submitted to: Monthly Weather Review

31 October, 2017

Corresponding author's address:

Jason P. Dunion

[Jason.Dunion@noaa.gov](mailto:Jason.Dunion@noaa.gov)

University of Miami/RSMAS/CIMAS

4600 Rickenbacker Causeway

Miami, FL 33149

## **Abstract**

The diurnal cycle of tropical convection and tropical cyclones (TCs) has been previously described in both observational and satellite based studies. This work expands on these earlier works and attempts to look for signs of the TC diurnal cycle (TCDC) in a hurricane nature run simulation and to characterize these signals in time and space. Based on previous studies that identified optimal conditions for the TCDC, a select period of the hurricane nature run is examined when the simulated storm was intense, in a low shear environment, and sufficiently far from land. When analyses are constrained by these conditions, marked radially propagating diurnal signals in radiation, thermodynamics, winds, and precipitation become evident in the model. The results of this work confirm previous studies that examined the TCDC using satellite data and has implications for numerical modeling of TCs and furthering our understanding of how the TCDC (and associated diurnal pulses) form, evolve, and possibly impact TC structure and intensity.

## 1. Introduction

Previous studies have documented diurnal variability of tropical oceanic convection (e.g. Gray and Jacobson 1977, Mapes and Houze 1993, Liu and Moncrieff 1998, and Yang and Slingo 2001) and the tropical cyclone (TC) upper-level cirrus canopy (e.g. Weikmann et al. 1977, Browner et al. 1977, and Kossin 2002). Dunion et al. (2014) examined a phenomenon described as the TC diurnal cycle (TCDC) and found cyclical pulses in the satellite infrared cloud field that propagate radially outward from mature TCs. These diurnal pulses begin forming in the storm's inner core near the time of sunset each day and continue to move away from the storm overnight, reaching areas several hundred kilometers from the circulation center by the following afternoon. Dunion et al. (2014) also presented a 24-h conceptual clock that describes the TCDC evolution and predicts the approximate arrival time (LST) of TC diurnal pulses at various radii from the storm center each day. This conceptual clock has utility for identifying the position and evolution of TC diurnal pulses in observational datasets and numerical simulations.

A study by Bu et al. (2014) used a pre-implementation of the 2013 operational HWRF model to examine aspects of cloud-radiative forcing (CRF) and how the modulation of atmospheric radiation by hydrometeors can influence the structure and intensity of TCs. Compared to runs with CRF turned off, simulations with CRF turned on (i.e., CRF-active) permitted hydrometeors to more consistently modulate longwave and shortwave radiative tendencies, especially in the TC cirrus outflow layer, with pronounced longwave cooling along the top of the outflow layer and weak longwave warming within the outflow layer. They found that CRF-active simulations produced storms with more convection and diabatic heating outside the eyewall, a wider eye, a broader wind field, and a stronger secondary circulation. Tang and Zhang (2016) used the Advanced Research version of the Weather Research and Forecasting Model (WRF ARW) to

examine the impacts of the diurnally varying radiation cycle on the formation, intensity, structure, and track of 2014 Hurricane Edouard. They found that diurnal effects varied depending on the intensity of the tropical disturbance or TC being simulated. During the genesis stage, nighttime destabilization of the atmosphere occurred via radiative cooling, which promoted deep convection near the disturbance center and eventually led to TC genesis. For TCs, they found that in the absence of nighttime conditions (i.e. in daytime-only simulations), storms fail to develop because of a lack of nighttime cooling and destabilization that typically enhances the primary storm vortex. They also concluded that nighttime destabilization was a key factor in stimulating convection outside the TC inner core and can eventually promote the development of outer rainbands and even increase the size of the storm.

Navarro and Hakim (2016) used a numerical simulation to examine the role of the diurnal cycle of radiation on axisymmetric hurricane structure. They found coherent diurnal signals in temperature, wind, and latent heating tendency fields that account for up to 62% of the variance in the TC outflow layer and 28% of the variance in the TC boundary layer. They hypothesized that the TCDC is a combined response from 2 distinct circulations in the storm: a radiatively driven circulation in the outflow layer due to absorption of solar radiation and a convectively driven circulation in the lower and middle troposphere due to anomalous latent heating that is linked to a diurnal cycle of anomalous convection.

The main goal of the current study is to examine an idealized hurricane nature run (Nolan et al. 2013) to look for signals of the TCDC in the model and to characterize these signals in time and space. Using criteria described in the following section, a select period of the nature run is examined when the simulated hurricane was intense, in a low vertical wind shear environment, and sufficiently far from land. When analyses are constrained by these conditions, marked diurnal

signals in radiation, thermodynamics, static stability, winds, and precipitation become evident in the simulation. Since the TCDC is a diurnal phenomenon, this study will begin with a focus on radiation in the hurricane nature run environment and will include analyses of outgoing longwave radiation (OLR), as well as shortwave, longwave, and total radiation tendencies. Discussion will then shift to include analyses of thermodynamics, static stability, winds, and finally precipitation. There are two aspects of the TCDC that are addressed by these discussions: 1) detection of the TCDC and radially propagating TC diurnal pulses (i.e. are TCDC signals that have been described and hypothesized in previous studies present in the hurricane nature run?); and 2) priming of the TC environment (i.e. are there diurnally varying aspects of the TC inner core and surrounding environment that promote the occurrence of convectively active, radially propagating TC diurnal pulses?). The findings that are presented confirm the satellite-based TCDC findings discussed by Dunion et al. (2014) and have implications for numerical modeling of TCs and furthering our understanding of how the TCDC (and associated diurnal pulses) forms, evolves, and possibly impacts TC structure and intensity.

## **2. Data**

The hurricane nature run that was examined in this study was simulated using the Weather Research and Forecasting (WRF) Model version 3.2.1 and is part of a larger 13-month joint observing system simulation experiment (OSSE) nature run that is described in detail by Nolan et al. (2013) and referred to as NRH1 in their paper. NRH1 spans a 13-day period from 29 July 0000 UTC – 11 Aug 0000 UTC 2005 and does not interact with land, unusually cold SSTs, or other synoptic weather systems during the portion of its life cycle that we examined. Track, minimum surface pressure, and maximum 10-m wind speed for the lifecycle of this simulated storm are

shown Fig. 1, during which time the radius of maximum winds contracts to a minimum radius of 45 km, later expanding to 60 km. The NRH1 9 km nested grid was utilized, which included 61 vertical levels (up to 50 hPa) and employed the WRF 6 class double-moment microphysics scheme (WDM6) [Lim and Hong, 2010], the RRTM-G schemes for both shortwave and longwave radiation (called every 6-min) [Iacono et al., 2008], and the Kain-Fritsch convective parameterization (Kain and Fritsch 1990). Additionally, the Yonsei University (YSU) planetary boundary layer scheme [Noh et al., 2003; Hong et al., 2006] was used for surface fluxes and turbulent mixing in the boundary layer (the “TC” option for formulas of surface exchange coefficients for momentum, heat, and moisture as a function of wind speed was employed). Finally, for parameterizing ocean cooling, the same mixed layer model as implemented in WRF 3.2.1 was used with an initial mixed layer depth of 25 m and stratification at the top of the thermocline specified as  $0.1 \text{ km}^{-1}$ .

The NRH1 exhibited a life cycle typical of a North Atlantic Cape Verde-type system, as it underwent genesis from an African easterly wave, intensified into a strong category 3 hurricane ( $\geq 49 \text{ m s}^{-1}$ ) from 05-07 Sept, and eventually recurved after reaching  $\sim 65^\circ\text{W}$ . The lifecycle of this sequence spans a 13-day period from 29 July 0000 UTC - 11 Aug 0000 UTC 2005. Dunion et al. (2014) found that the TCDC was most pronounced in mature hurricanes (Saffir-Simpson intensity of category 2 or higher ( $43 \text{ m s}^{-1}$ )) that were in relatively low shear environments ( $\leq 7.5 \text{ m s}^{-1}$  of 200–850-hPa vertical wind shear) and located  $\geq 300 \text{ km}$  from land and constrained their storm sample accordingly. This study uses these same thresholds to identify the portion of the NRH1 lifecycle that would be most conducive for TCDC processes. Figure 1 shows the track and intensity for the 13-day NRH1 simulation period and indicates that the storm met the minimum distance to land threshold for the entire period and that the intensity requirement was attained from

days 5-10. Finally, Nolan et al (2013) showed that the vertical wind shear affecting NRH1 during this 5-day period never exceeded  $7.5 \text{ m s}^{-1}$ . Therefore, days 5-10 (03 Aug 0000 UTC - 08 Aug 0000 UTC) of the NRH1 simulation were searched for signs of the TCDC.

### 3. Results

#### 3.1 Radiation

##### *a. Outgoing Longwave Radiation (OLR)*

OLR represents the total longwave infrared energy radiating from the Earth to space and is affected by surface temperature and emissivity, atmospheric temperature, water vapor profile, and cloud cover. It is expected that OLR should correlate highly with the findings of Dunion et al. (2014) that used the 10.7 and 10.8  $\mu\text{m}$  channels on the GOES and Meteosat satellites to detect the TCDC and associated diurnal pulses propagating away from the storm. Figure 2 shows a Hovmoller of OLR for the first 10 days of the life cycle of NRH1 before it began to recurve into the mid-latitudes and weaken below category 2 intensity. This figure reveals a marked diurnal oscillation in the OLR pattern that becomes established at a radius (R) range of  $\sim 150\text{-}450 \text{ km}$  beginning on day 5 (03 Aug) and continues through day 10 (08 Aug), the only period in the NRH1 when all three previously described TCDC criteria are satisfied. This figure also suggests that the OLR signal appears to propagate away from the storm each day. Figure 2 includes the same OLR Hovmoller for only the 5-day study period (03-08 Aug) and emphasizes the diurnal fluctuations in OLR, especially at  $R=150+$  km from the storm center. Diurnal fluctuations of  $\pm 20\text{-}60 \text{ W m}^{-2}$  are evident at  $R=150\text{-}250 \text{ km}$ , while larger fluctuations of  $\pm 45\text{-}70 \text{ W m}^{-2}$  occur at  $R=350\text{-}450 \text{ km}$ . These fluctuations indicate that a distinct radially propagating OLR diurnal cycle signal is evident in NRH1 with  $R=150\text{-}450 \text{ km}$  OLR maxima from  $\sim 0000\text{-}0600 \text{ UTC}$  ( $\sim 2000\text{-}0200 \text{ LST}$ ) and OLR

minima from ~1400-2000 UTC (~1000-1600 LST) each day. The diurnal timing of these longwave infrared peaks and troughs and radial propagation speed ( $5-10 \text{ m s}^{-1}$ ) is very similar to the TCDC described by Dunion et al. (2014). Given the location of NRH1 over the ocean throughout the simulation, this diurnal infrared radiation signal is likely arising through a combination of variations in atmospheric temperature, moisture, and cloud cover. Several of the sections that follow include detailed analyses of these various components of OLR.

*b. Shortwave, Longwave, and Total Radiation*

Since the TCDC is a diurnal phenomenon that has been linked to the solar cycle (Dunion et al. 2014), analyses were made of shortwave, longwave, and total radiation tendency for the NRH1 domain from 03-08 August at 200, 700, and 925 hPa (Fig. 3). Not surprisingly, the shortwave tendencies show regular oscillations of net warming that are associated with the daily solar cycle and influenced by the 3-dimensional distribution of clouds in the storm. For example, near the outflow layer (~200 hPa), maximum daytime warming takes place from  $R \sim 50-300 \text{ km}$  due to the presence of cirrus clouds (i.e. elevated ice mixing ratio in the outflow layer; Fig. 4). There is also little warming inside of  $R \sim 50 \text{ km}$  due to the relatively cirrus-free eye region of the storm and a general trend for reduced peak warming with increasing radii (outside of the eye;  $R > 50 \text{ km}$ ), which is due to the presence of generally less optically thick clouds with increasing radius from the storm, as suggested by Fig. 4. Although shortwave warming ( $\sim 0.3-1.0 \text{ K h}^{-1}$ ) occurs near the top of the TC (e.g. 200 hPa) from  $R \sim 25-450 \text{ km}$ , lower to middle levels (e.g. 700 and 925 hPa) experience near zero shortwave warming during the day from just outside the eye to  $R \sim 150-250 \text{ km}$  where ice mixing ratio suggests the presence of a diurnally varying and optically thicker cirrus outflow layer each afternoon (presumed from analyses of

OLR in Fig. 2 and ice mixing ratio Fig. 4) that would act to block incoming shortwave radiation (Figs. 4 and 5).

Although longwave infrared tendencies are generally producing a net cooling in the upper levels across the NRH1 domain, there are preferred times of day when the cooling rate appears to be more pronounced. At 200 hPa, peak longwave cooling occurs in the daytime, reaches a minimum at night, and is correlated with higher values of ice mixing ratio (Fig. 5). Although the cloud-free atmosphere is relatively transparent to longwave IR radiation emitted from the Earth, the TC cirrus outflow layer becomes increasingly efficient at absorbing this longwave radiation as these daytime radial surges of high cirrus occur and the layer becomes optically thicker. As indicated by the Stefan-Boltzman Law,

$$E = \sigma T^4 \quad (1)$$

where  $E$  is the total energy radiated per unit surface area of a black body across all wavelengths per unit time,  $\sigma$  is Stefan–Boltzman constant ( $5.670373 \times 10^{-8} \text{ W m}^{-2} \text{ K}^{-4}$ ), and  $T$  is the blackbody's thermodynamic temperature, the energy emitted by an object is proportional to the fourth power of its temperature. In NRH1 simulation, the longwave IR energy that is absorbed by the cirrus outflow layer is re-emitted both back to the Earth and to the top of the atmosphere and because these cirrus clouds are high (e.g.  $\sim 300$ - $150$  hPa or  $\sim 9.5$ - $14$  km), and therefore cold, the longwave energy that they radiate to the top of the atmosphere is lower than it would be in the absence of cloud or in an optically thinner layer of cloud. Figure 4 indicates that in the late morning/early afternoon, the radial extent of the TC cirrus canopy is greater and contains ice mixing ratio values from  $z \sim 6$ - $15$  km that are a factor of 2-10 times higher than they are in the evening. The optically thicker surges of cirrus clouds from the late morning to early afternoon could explain the daytime peak longwave cooling patterns seen in the upper levels each day (Figs. 4 and 5).

It is possible that rapid cooling at the level of the cirrus outflow layer near and after sunset each day could promote conditions that are conducive for trapping gravity waves that emanate from the TC inner core (e.g. Metcalf 1975 and Crook 1988). Although the resolution of the NRH1 simulation that was used (9 km nested grid; see section 2.1.2) may be inadequate to completely resolve gravity waves in the simulated TC (e.g. perturbations in fields of potential temperature and vertical winds), the feature described in the NRH1 vertical wind analyses in section 3.3d is noteworthy. This feature is seen as a large, radially propagating, and relatively narrow ring of enhanced vertical wind that is highly circular in shape.

The radius-height cross-sections of total, shortwave, and longwave radiation tendency in Figs. 6-8 show the 3-dimensional radiation profiles of the NRH1 and emphasize radiative processes of the background TC environment that may be priming the environment to support TCDC and TC diurnal pulses. These figures includes two elevated regions, A and B, that extend from 3-13 km in the vertical and span from  $R=50-200$  km and  $R=200-400$  km in the horizontal respectively. The vertical extent of the two regions was chosen to capture 1) the lower extent of persistent warming that occurs throughout the day from  $R\sim 50-450$  km; and 2) the extreme upper and lower bounds of the level of neutral buoyancy (LNB) that were found in the NRH1 (describe in section 3.3c). The horizontal extent of these two regions was selected to highlight the regions of the TC inner core ( $R\leq 150-200$  km) versus the surrounding environment ( $R\sim 200-450$  km) and highlight a persistent low-level layer of net warming from  $R\sim 50-200$  km that may be acting to stabilize the inner core and near-inner region of the TC. Regions A and B may represent key areas of the storm where radiation tendencies can lead to marked diurnal fluctuations in static stability (e.g. the LNB and convective available potential energy (CAPE)) and are discussed further in section 3.3c. While region A corresponds to the approximate radius range of TC diurnal pulse

initiation that was noted by Dunion et al. (2014), both regions experience patterns of net radiation tendencies that may be important for TCDC processes. For Figs. 6-8, nighttime is ~2100-0300 LST, dawn is ~0600 LST, daytime is ~0900-1500 LST, and dusk is ~1800 LST. Specific conclusions related to the analyses of radiation in the NRH1 include:

1. Shortwave warming during the daytime and longwave cooling at night are preferentially occurring in the cirrus outflow layer (i.e. areas of enhanced ice mixing ratio, Fig. 4). Since the TC outflow layer lowers with increasing radius, relatively more shortwave warming and longwave cooling occurs in the middle to upper levels of region B compared to region A.
2. During the day, shortwave warming is greater than opposing longwave cooling in the upper few kilometers of regions A and B ( $z \sim 10-13$  km) and could be a time when the LNB lowers and CAPE is reduced. This may be a key process influencing the daytime evolution of the TCDC and will be discussed more **section 3.3c**.
3. During the nighttime, longwave cooling dominates the upper few kilometers of regions A and B ( $z \sim 8-13$  km) and could be a time when the LNB rises and CAPE increases. This may be a key process influencing the nighttime evolution of the TCDC and will be discussed more **section 3.3c**.
4. Region A has a layer of persistent net warming ( $\sim 0.1-0.3$  K  $\text{hr}^{-1}$ ) from  $z \sim 4-6$  km that occurs all day, with slightly more warming during the daytime. This warming is occurring just above the melting level and is coincident with the base of the elevated ice mixing ratio shown in Fig. 4 ( $>0.02$  g  $\text{kg}^{-1}$ ). This region of relatively high ice content is likely absorbing longwave IR radiation being emitted from the Earth's surface and could be acting to

consistently lower the LNB and reduce CAPE in this area within and just outside the TC inner core.

5. Region B also exhibits a layer of lower level net warming ( $\sim 0.1-0.4 \text{ K hr}^{-1}$ ) that persists throughout the day, but unlike the layer in region A, this layer slopes upward with radius from  $z \sim 4-6 \text{ km}$  at  $R=200 \text{ km}$  to  $z \sim 7-11 \text{ km}$  at  $R=450 \text{ km}$  and appears to be linked to the upward sloping anvil cloud base that is evident in the Fig. 4 cross-sections. The time of peak net cooling (local midnight) and warming (early to late afternoon) likely represent times with elevated LNBs and increased CAPE and lower LNBs and decreased CAPE respectively and will be discussed further in **section 3.3c**.

The aforementioned conclusions of radiation tendencies suggest that the inner 400 km of the NRH1 experiences marked diurnal fluctuations in radiation tendencies that are more pronounced at larger radii (e.g. in region B). These diurnal fluctuations could generate reduced static stability (i.e. a lower LNB and reduced CAPE) in the storm environment that peak from around dusk until dawn and will be discussed further in **section 3.3c**. Strikingly similar radiation tendencies to those shown in Figs. 6-8 were noted throughout the study period (not shown), suggesting that the 3-dimensional variability of shortwave, longwave, and total radiation tendencies may create an environment each day that primes, or pre-conditions, the TC environment to support the TCDC and associated radially propagating diurnal pulses that have been previously documented. This priming is accomplished via cooling of the middle to upper level environmental profile that would act to destabilize the environment and increase Inertial Available Kinetic Energy (IAKE, Mecikalski and Tripoli 1998), which would favor upper-level outflow release. The radiation tendencies shown here (i.e. negative radiation tendencies that are favored at  $R \geq 150-200 \text{ km}$  ( $\sim 2.5-4.5$  times the radius of maximum winds and radially outside of region A) may also help

explain why the TCDC seen in both satellite imagery (e.g. Dunion et al. 2014) and in the NRH1 appear to begin each day near  $R \sim 150\text{-}200$  km. The TCDC may either be undetectable or simply not originating from the TC inner core region (e.g.  $R \sim \leq 150$  km; Rogers et al. 2012). Instead, diurnal radiation tendencies in mature TCs may come together in such a way to preferentially trigger convection in this region of the storm each night near and after the time of local sunset. This will be explored further in the **section 3.3c** analyses of static stability.

## 3.2 Thermodynamics and Stability

### *a. Potential Temperature*

Analyses of potential temperature ( $\theta$ ) were conducted to search for signs of the TCDC in the NRH1 thermodynamic fields. These analyses reveal distinct diurnal signals at various atmospheric levels (e.g. 200, 700, and 925 hPa, and the near-surface) and radii. At upper levels (e.g. 200 hPa), there is no robust diurnal signal in the inner 150 km of the storm. However, there is a distinct diurnal  $\theta$  pattern just outside of 150 km with maxima around local noon and minima around local midnight (Figs. 9 and 10). The  $\theta$  patterns in this region of the storm correspond to the outer edge of the TC inner core, are correlated with upper level shortwave and total radiation tendencies, and are negatively correlated with longwave radiation tendencies (Fig. 3). These diurnal  $\theta$  patterns also appear to be propagating radially away from the TC (Fig. 9) and are closely matched in time and space with OLR (Fig. 2) and ice mixing ratio (Fig. 4). This suggests that diurnal variability at the level of the TC cirrus canopy is driving the upper-level  $\theta$  patterns at  $R \sim 150\text{-}450$  km. Values of  $\theta$  at upper levels begin cooling each afternoon and reach a minimum around local midnight, which implies that this region of the storm experiences regular occurrences of destabilization via cooling of the environmental profile in the upper-levels (e.g. an elevated

LNB and higher CAPE) from the late afternoon into the evening, which could help promote convection locally (Figs. 9 and 10).

The middle levels (e.g. 700 hPa) of the NRH1 TC do not exhibit robust diurnal  $\theta$  fluctuations in the inner 300 km of the storm (Figs. 9 and 10). There is a modest diurnal signal from R~300-450 km with peak warming (cooling) in the evening to local midnight (pre-dawn hours) and  $\theta$  fluctuations of ~0.5-1 K.

Diurnal  $\theta$  patterns are quite evident in the lower levels (e.g. 925 hPa and 40 m) of the NRH1 TC environment, particularly from day 2-5 (05-08 Aug, Figs. 9 and 10). At 925 hPa and especially 40 m, the diurnal  $\theta$  signals appear to be propagating away from the storm each afternoon. The 40-m near-surface diurnal fluctuations range from ~0.5-1.5 K and suggest that some kind of outflow boundary that is bringing cooler air to the surface may be propagating away from the storm from the late morning to afternoon each day and occur within 6 hours of corresponding temperature minima in the upper levels (e.g. 200 hPa).

*b. Moisture (mixing ratio)*

In order to examine how the TCDC might be affecting the moisture field of the simulated TC and to identify possible signals related to diurnal moisture variability in the storm, mixing ratio is examined. The NRH1 TC exhibits distinct diurnal signals in mixing ratio at all levels (Figs. 11 and 12). At upper levels (e.g. 200 hPa), these oscillations are most pronounced from R=150-450 km, peak around local noon at inner radii, and appear to slowly propagate away from the storm during the afternoon. Variations in 200 hPa mixing ratio showed a distinct diurnal pattern that is similar to previously shown patterns of OLR and potential temperature, suggesting that the TCDC signal is characterized by marked changes in both temperature and moisture.

At middle levels of the NRH1 (e.g. 700 hPa), there is a less defined pattern of diurnal mixing ratio throughout the domain (Figs. 11 and 12). However, at R=150-300 km, there are prominent middle level diurnal peaks in mixing ratio that occur in the late evening through early morning hours each day. These maxima are regularly interspersed by ebbs in mixing ratio that occur in the middle to late afternoon, are 0.5-2.5 g kg<sup>-1</sup> dryer, and appear to be anti-correlated in time with the upper level values (e.g. 200 hPa).

The lower levels (e.g. 925 hPa and 40-m) show a robust TCDC of mixing ratio that tends to be at a minimum in the late morning to late afternoon hours and are most evident from R~100-300 km (Figs. 11 and 12). These minima are regularly interspersed by periods of mixing ratio peaks that are significantly moister (~0.5-2.5 g kg<sup>-1</sup>). The patterns of mixing ratio minima appear to be more pronounced than the maxima and exhibit signs of radial propagation that is particularly pronounced from R=150-350 km. Dunion et al. (2014) noted that large outflow boundaries denoted by arc clouds that are hundreds of kilometers in length tend to form along the leading edge of TC diurnal pulses. These outflow boundaries are associated with convectively-driven downdrafts that originate in the lower to middle levels (e.g. 600-800 hPa) and bring relatively cool, dry air down to the near-surface. Although analyses of  $\theta$  do not show discernable signatures of convectively-driven downdrafts, radius-height analyses of the NRH1 (shown in **section 3.4b**) indicate that diurnal signals of depressed mixing ratio are evident from ~4 km to the surface and are approximately timed to the TC diurnal pulses described by Dunion et al. (2014). This suggests that the diurnal mixing ratio patterns evident in the lower to middle levels of the NRH1 may, in fact, be linked to a squall line feature with outflow boundaries that propagate away from the NRH1 storm each day and will be discussed more in **sections 3.3d and 3.4c**.

*c. LNB and Convective Available Potential Energy*

CAPE is defined as the amount of energy a parcel of air would have if lifted a certain distance vertically through the atmosphere up to the LNB. Calculations of CAPE in this study assume that a surface parcel is represented by the mean temperature and moisture in the lowest 500 m of each sounding profile that was computed across the NRH1 domain and include irreversible moist-adiabatic processes. CAPE exhibits a distinct TCDC pattern and similar to other parameters that have been previously discussed, a diurnal CAPE signal is evident throughout the study period, and is especially pronounced from 05-08 Aug (Figs. 13 and 14). CAPE displays TCDC signals that are most pronounced from R~150-300 km, has maximum values in the early morning hours between approximately local midnight and 0900 LST, minimum values from the late morning to late afternoon, and consistently low values ( $\sim 0-500 \text{ J kg}^{-1}$ ) inside of R~150 km. Diurnal variations in radiation tendency at critical levels appear to be impacting the environmental temperature profile and resulting LNB. The TCDC signals in CAPE in Figs. 13 and 14 appear to be in phase with the patterns of middle to upper-level ( $z\sim 4-10 \text{ km}$ ) total radiation tendencies discussed in **section 3.1** and shown in Fig. 3 and Figs. 6-8. Maxima in CAPE tend to occur during and shortly after periods of overnight net cooling, while minima occur during and shortly after periods of daytime net heating, suggesting that radiation tendencies in the middle to upper-levels are an important control on diurnal fluctuations of CAPE. It was hypothesized in section 3a (ii) that varying radiation tendencies at various radii from R=50-400 km may have important implications on the LNB and hence CAPE in the NRH1 environment. Throughout the study period, the radius range of R~50-100 km has little to no CAPE ( $0-500 \text{ J kg}^{-1}$ ) and LNBs as low as 600-800 hPa, which may be related to persistent warming that occurs in the layer from  $z\sim 4-6 \text{ km}$  during both the daytime and nighttime (Fig. 6). The magnitude of this warming does fluctuate

diurnally and appears to be contributing to the diurnal variability of CAPE (Figs. 13 and 14) and the LNB (Fig. 14). At radii of  $\sim 150\text{-}350$  km, CAPE and the LNB fluctuate diurnally by as much as  $1500 \text{ J kg}^{-1}$  and 450 hPa respectively and are remarkably in phase throughout the day. As the LNB pressure level increases (decreases), corresponding CAPE values decrease (increase). It is also evident that at  $R=150\text{-}200$  km, there is a general linear decrease (lowering) of CAPE (the LNB) as the simulation progresses. Over time, priming of the atmosphere becomes somewhat less favored at these radii, especially at  $R=150$  km.

Figure 15 shows the 3-hourly progression of CAPE in the NRH1 inner core and surrounding environment from 06 Aug 0200 LST to 07 Aug 0200 LST. In the early morning of 06 Aug (0200-0500 LST), a fairly symmetric region of very low CAPE values ( $\sim 0\text{-}500 \text{ J kg}^{-1}$ ) exists in the inner  $\sim 150\text{-}200$  km of the storm and is immediately surrounded by areas of higher CAPE ( $\sim 1500\text{-}3000 \text{ J kg}^{-1}$ ) that extend out to the edges of the NRH1 domain. This annulus of inner core low CAPE begins to radially expand near the time of sunrise ( $\sim 0530$  LST) and continues to grow through the early to late afternoon, eventually reaching  $R\sim 300\text{-}400$  km. The expanding area of low CAPE during the daytime also concurs with the Fig. 6 depiction of marked daytime (nighttime) radiational warming (cooling) in the middle to upper levels ( $z\sim 6\text{-}12$  km) and corresponding  $0.5\text{-}3.5$  K diurnal fluctuations in  $\theta$  shown in Figs. 9 and 10. Periods of cooling would act to raise the LNB, reducing the total integrated area being used to calculate CAPE, hence, reducing local values of CAPE. Starting in the early evening near the time of local sunset (i.e.  $\sim 2000$  LST), the low CAPE annulus begins to dissipate along its periphery and continues to wane into the late evening until around local midnight. By the early morning hours the next day (07 Aug 0200 LST), the shrinking annulus of low CAPE appears to stabilize and once again extends to a radius of only  $\sim 150\text{-}200$  km. Near and just outside this radius range, CAPE values increase

from  $\sim 0-500 \text{ J kg}^{-1}$  to as high as  $2500 \text{ J kg}^{-1}$  in just a few hours leading up to 0200 LST. This period of enhanced CAPE after sunset in the 150-200 km radius range could be related to the middle to upper level cooling noted in the corresponding areas of regions A and B of Fig. 6. The  $0-0.5 \text{ K hr}^{-1}$  cooling rates that were noted in this area just outside the inner core of the TC would promote reduced lapse rates and increased CAPE locally.

Around the time of local sunrise and through the afternoon to the time of sunset the following day, the annulus of low CAPE once again continues a cycle of radial expansion (not shown). A nearly identical sequence of a diurnally expanding and contracting annulus of low CAPE was also evident the day prior (05-06 Aug, not shown). It is hypothesized that radiational warming and cooling in the TC environment immediately surrounding the TC inner core (e.g.  $R=150-350 \text{ km}$ ) are producing striking fluctuations in the LNB each day. These variations in LNB are, in turn, driving diurnal fluctuations in CAPE that dramatically alter the static stability in the NRH1 TC environment and could be a trigger for the formation of diurnal pulses that have been previously discussed. Radiative warming and cooling associated with the TC cirrus canopy and radially sloping TC anvil are hypothesized to be a driving mechanism for the marked diurnal fluctuations in the LNB and CAPE that have been found could help prime the TC environment to support the development of convectively active TC diurnal pulses in the region of the storm just outside the inner core at  $R\sim 150-300 \text{ km}$ ).

### **3.3 Wind**

#### *a. Surface (10-m) Wind*

Analyses of 10-m surface winds in the NRH1 were performed to assess the relevance of the TCDC to TC intensity and structure. Surface winds show a clear diurnal signal at radii ranging

from  $\geq 50$  km (Figs. 16 and 17). In the inner 200 km of the storm, surface winds tend to peak from the late evening to early morning hours and ebb from the afternoon to late evening. These wind speed oscillations range from  $\sim 0.5$ - $2.5$   $\text{m s}^{-1}$  and tend to be larger with increasing radii. Although the radial and tangential components of the surface wind both exhibit diurnal fluctuations, radial wind has particularly pronounced signals (Fig. 16), suggesting that the diurnal fluctuations of surface wind speed shown in Fig. 17 are largely attributable to ebbs and flows in radial winds at the surface. These diurnal fluctuations appear to be most pronounced at  $R \sim 150$ - $350$  km where diurnal oscillations in the magnitude of radial inflow are as high as  $4$ - $6$   $\text{m s}^{-1}$ . The tendency for surface wind diurnal oscillations to be more pronounced at larger radii has implications for TC structure (e.g. significant wind radii). This is particularly so for the radii of 34 and 50 kt winds, which in the North Atlantic, average  $\sim 155$  km and 85 km respectively (Demuth et al 2006).

Analyses of 10-m surface winds show a strong diurnal signal with periods of stronger winds and more vigorous low-level inflow in the early morning hours that are interspersed with periods of weaker winds and reduced lower level inflow from the mid morning to early afternoon. These trends in surface wind suggest potential links between the TCDC and TC intensity and structure.

*b. Radial Wind (Near Surface to Upper-Level)*

Radial wind ( $V_r$ ) tendencies in the NRH1 exhibit distinct diurnal patterns throughout the troposphere (Fig. 18). In the upper troposphere (e.g. 200 hPa), there appear to be daily bursts of outflow outside of  $\sim 100$ - $150$  km that develop in the early morning hours each day and steadily propagate away from the storm (at speeds similar to those described by Dunion et al. (2014), reaching  $R=450$  km in the afternoon. These daily maxima in outflow steadily strengthen through

the study period, are strongest from  $R \sim 200\text{-}400$  km, and have peak values of  $\sim 15\text{-}20$   $\text{m s}^{-1}$ . The 200 hPa radial outflow bursts are also regularly interrupted by outflow minima that peak from the late evening to early morning hours each day and are roughly a factor of two weaker (Fig. 18). These surges in  $V_r$  are coincident in time with the diurnal patterns shown in OLR (Fig. 2), as well as 200 hPa ice mixing ratio,  $\theta$ , and mixing ratio, suggesting that TC diurnal pulses are associated with marked upper-level signals in both thermodynamics and kinematics. Although there does not appear to be a robust upper-level diurnal signal in radial winds inside of  $\sim 150$  km, diurnal outflow variability beyond this radius is marked and may have important implications for TC intensity and structure.

In the middle levels of the atmosphere (e.g. 700 hPa), there is a distinct diurnal pattern of enhanced inflow ( $2\text{-}5$   $\text{m s}^{-1}$ ) each day that peak in the early morning and are concentrated at  $R = 150\text{-}300$  km (Fig. 18). These inflow surges occur prior to and radially inward of the 200 hPa outflow bursts that were previously discussed and are interspersed by periods of weak or even near-zero inflow that peak from the late evening to early morning hours each day. Finally, on the inside edge of these inflow bursts ( $R \sim 25\text{-}150$  km) there are areas of outflow ranging from  $0.5\text{-}3$   $\text{m s}^{-1}$ . The diurnal patterns of inflow and outflow suggest that there are favored times of day (approximately midnight to 0600 LST) when local middle level convergence is maximized and could represent times when the TC is more susceptible to middle level ventilation (i.e. the flux of cooler, drier middle level air into a TC; Tang and Emanuel 2012).

At the lower levels, diurnal tendencies of  $V_r$  are evident from  $R = 100\text{-}450$  km (Fig. 18). Peak inflow ( $\sim 12\text{-}18$   $\text{m s}^{-1}$ ) tends to occur in the late evening to early morning hours and is interrupted by periods of relatively weaker inflow ( $5\text{-}12$   $\text{m s}^{-1}$ ) that reach a minimum from the late morning to afternoon hours. These peaks and ebbs in low-level  $V_r$  appear to propagate away from

the storm each day and the  $V_r$  magnitude steadily increases as the simulation progresses and the storm grows and intensifies. The flow patterns suggest that TC inflow and surface fluxes (not shown) are maximized just before and after local midnight from  $R=100-200$  km and peak at larger radii ( $200+$  km) in the early to late morning. It should be noted that diurnal peaks in low-level inflow coincide with peaks in low-level moisture that were discussed in [section 3.2](#) and shown in Fig. 11.

The phasing of maximum near-surface inflow and maximum upper-level outflow are slightly offset in time (Fig. 18). The maximum near-surface inflow occurs in the late evening to early morning hours, while the peak upper-level outflow tends to occur in the mid-morning to late afternoon. This temporal offset of several hours suggests that surges in low-level inflow proceed/follow surges in upper level outflow and that the mechanism(s) driving the TCDC do not initiate radial flow simultaneously throughout the depth of the storm. Perhaps radiative effects initiate enhanced outflow near the level of the outflow layer each day and there is a lag between this onset and the onset of enhanced radial inflow.

*c. Tangential Wind (Near Surface to Upper-Level)*

Tangential winds ( $V_t$ ) in the NRH1 exhibit marked diurnal signals throughout the troposphere and are most pronounced in the upper levels (e.g. 200 hPa). Figure 19 shows the occurrence of episodic oscillations in upper-level  $V_t$  that are particularly apparent from  $R=150-450$  km. Peaks in upper-level  $V_t$  occur in the middle to late afternoon at  $R=300$  km and in the late afternoon to early evening at  $R=450$  km and similar to radial wind,  $V_t$  peaks are regularly interrupted by lulls that are a factor of 1.5-5 times weaker at radii ranging from 200-450 km.

The middle levels (e.g. 700 hPa) of the NRH1 show a relatively more muted  $V_t$  diurnal signal that is more pronounced at larger radii (Fig. 19). This figure indicates subtle diurnal oscillations with maxima that occur in the early to middle afternoon and minima around local midnight. Lower level (e.g. 925 hPa and 40 m) diurnal fluctuations in  $V_t$ , although not as pronounced as at upper levels, are clearly evident from R=150-450 km and are particularly robust at R=300 km (Fig. 19). Here, peak values of  $V_t$  tend to occur in the late morning to early afternoon and reach a minimum in the evening, propagating at speeds similar to those described by Dunion et al. (2014). These analyses suggest that there are favored times of day for maximum and minimum values in the magnitude of  $V_t$  in the upper, middle, and lower levels of the NRH1 TC.

#### *d. Vertical Wind*

Vertical wind ( $w$ ) in the NRH1 shows a distinct diurnal pattern that appears to propagate away from the storm each day at speeds similar to previously discussed variables (Fig. 20). At upper levels (e.g. 200 hPa), peaks in  $w$  appear at R=150-200 km in the late morning and propagate to peripheral radii through the early to late afternoon. Maxima in  $w$  range from  $\sim 0.1-0.5 \text{ m s}^{-1}$ , while interspersed minima reach magnitudes close to zero and are occasionally even negative (Fig. 20). Although the diurnal signal of  $w$  is evident at R $\sim$ 150-450 km, this figure shows that the magnitudes of the peaks are highest at closer radii and lower with increasing radius from the storm.

Diurnal signals of  $w$  in the lower to middle levels are less defined than in the upper levels (Fig. 20). However, 2-dimensional map analyses of  $w$  throughout the study period indicate that this parameter marks the position of the diurnal pulses quite clearly and is seen as a narrow ( $\sim 10-20$  km wide) ring of enhanced  $w$  that radially propagates away from the storm and has a squall line-like appearance (Fig. 21). The relatively limited radial width of this feature coupled with

slight azimuthal asymmetries in the NRH1 diurnal pulse signal (i.e. enhanced  $w$ ) may be somewhat muting the  $w$  signal when it is azimuthally averaged (e.g., Fig. 20). Figure 21 shows a 6-hourly progression of a diurnal pulse on 06 Aug from 0600 UTC (0200 LST) to 1800 UTC (1400 LST) and shows a semi-circular signal in  $w$  that is propagating away from the storm each day, reaches  $R \sim 300$  km in the afternoon, and is evident through a deep layer of the troposphere from 150-925 hPa (not shown). This figure suggests that diurnal pulses are associated with distinct peaks in  $w$  with updrafts that range from  $\sim 1-3$  m s<sup>-1</sup> and trailing 0.5-2 m s<sup>-1</sup> downdrafts that appear to be favored behind the diurnal pulse. The couplets of highly symmetric updrafts and downdrafts suggest that these diurnal pulses may be a squall line feature or gravity wave moving/propagating away from the storm each day. The timing of these propagating diurnal pulse signals in  $w$  also correspond well with the TCDC clock presented by Dunion et al. (2014). Similar analyses made on 04, 05, and 07 Aug (not shown) indicate a nearly identical diurnal pulse signature in  $w$  that is highly symmetric and is also propagating away from the storm. Analyses of  $w$  support one of the hypothesized TCDC mechanisms discussed in Dunion et al. (2014): convectively-driven atmospheric gravity waves.

### **3.4 Precipitation**

#### *a. Rain Rate*

Rain rate shows a distinct TCDC pattern and is especially evident from  $R=100-300$  km (Figs. 22 and 23). Similar to analyses of temperature, moisture, and winds, radially propagating signals in rain rate can be seen throughout the study period, but are particularly robust from 05-08 Aug (Fig. 22 and 23). Peaks occur in the late evening to early morning hours in the inner core (e.g.  $R=100-150$  km) and in the early to late morning farther from the storm (e.g.  $R=200-250$  km,

Fig. 23). Conversely, rain rate minima occur in the late morning to middle afternoon at R=100-150 km and in the late afternoon to late evening at R=200-250 km. These patterns in rain rate suggest that the TCDC may have important implications for quantitative precipitation forecasting and TC structure.

*b. Simulated Radar Reflectivity*

Analyses of simulated radar reflectivity show a robust propagating diurnal signal that extends throughout the troposphere (Fig. 24). Diurnal oscillations in this parameter range from ~10-30 dBZ and are especially evident from R=100-300 km. Not surprisingly, these patterns of reflectivity closely resemble those of rain rate and given the diurnal signal of reflectivity, it is plausible that aircraft equipped with radar (e.g. C-band or X-band Doppler) could be used to track the evolution of the TCDC in the future. Additionally, given the common practice of empirically estimating rainfall from land-based radar, the TCDC could be an important consideration regarding the analysis of quantitative precipitation forecasts for landfalling TCs.

*c. Q-Condensate*

Figure 25 shows NRH1 azimuth-radius analyses of Q-condensate and vertical wind during the most pronounced day of diurnal reflectivity fluctuations (06 Aug). This figure suggests that an area of enhanced moisture and vertical winds forms outside the eyewall (R~75-150 km) around local midnight that day. The feature appears to be elevated above the surface, has a vertical extent of ~2-14 km, and clearly propagates away from the storm throughout the day, reaching radii of approximately 200, 250, and 300 km at 0600, 1200, and 1800 LST respectively. This region of enhanced moisture and vertical winds may, in fact, be linked to a diurnal pulse that is propagating

away from the storm and during the afternoon, becomes coupled with a trailing downdraft and area of suppressed low-level moisture. The area behind the diurnal pulse extends from the surface to  $\sim 3$  km and may be the signature of a cold pool. In fact, the entire propagating feature (TC diurnal pulse and cold pool) looks remarkably similar to a squall line. If TC diurnal pulses do indeed behave like squall line features that propagate away from the storm each day, some kind of common lifting mechanism, such as a gravity wave, frontal feature, or outflow boundary is suggested. Also, since squall lines develop in regions of optimal moisture, stability, and lift, it is possible that the priming of the environment just outside the inner core ( $R \sim 150$ - $350$  km) during the nighttime that was discussed in **section 3.3c** (i.e. elevated LNB and enhanced CAPE) could support the existence of a convectively active, long lived (several hours) squall line feature. Finally, squall lines are partly sustained via the production of lift via outflow boundaries. Dunion et al. 2014 noted that arc clouds (i.e. outflow boundaries) often appear to form along the leading edges of TC diurnal pulses, which further supports this idea that TC diurnal pulses associated with the TCDC behave like squall lines. These ideas will be explored in future work. Whatever this feature is, it repeats over multiple days of the NRH1 study period and appears to have origins in a deep (but elevated) layer at radii where radiation tendencies support reduced static stability and increased IAKE near and after sunset each day. The TCDC conceptual clock presented by Dunion et al. (2014) also suggests that as this feature propagates away from the storm during the early to late morning, it is located at  $R \sim 200$ - $300$  km. Analyses of the LNB (**section 3.2c**, Fig. 14) indicate that this timing coincides with diurnal minima in LNB heights ( $z \sim 500$ - $600$  hPa) in this region of the peripheral TC environment, which could act to limit its vertical extent as it propagates away from the storm. Although the exact mechanism causing the diurnal features described above is not

clear, their regular diurnal occurrence does suggest that radiation tendencies that are being driven by the solar cycle may be a key controlling factor.

#### **4. Conclusions**

The goal of this study was to examine a hurricane nature run (NRH1) simulation to look for signals of the TC diurnal cycle (TCDC) in the model and characterize these signals in time and space. This work finds a marked radially propagating diurnal signal in a simulated TC that becomes robust when the storm reaches category 2 intensity (i.e.,  $\geq 43 \text{ m s}^{-1}$ ), is embedded in a low vertical wind shear environment (i.e.,  $\leq 7.5 \text{ m s}^{-1}$ ), and is sufficiently removed from land (i.e.,  $\geq 300 \text{ km}$ ). When these thresholds described by Dunion et al. (2014) are satisfied, various diurnal signals in thermodynamics, static stability, winds, and precipitation become apparent in and around the storm environment. Details of these signals are discussed in the context of both time and space and may be applicable to other simulated TCs where the employed model includes a solar cycle and the simulated storm satisfies the aforementioned conditions. Figure 26 presents a schematic that summarizes diurnal background states for parameters of radiation, thermodynamics, kinematics, and precipitation that were discussed in this chapter. This schematic highlights relative diurnal trends of these parameters at various levels in the evening to early morning hours when the TCDC and TC diurnal pulses are first beginning to evolve versus the mid-morning to afternoon hours, when TC diurnal pulses have propagated several hundred kilometers from the NRH1 inner core. Figure 27 presents a TCDC-centric schematic summarizing the daytime evolution of TC diurnal pulses, seen as radially propagating squall line features with associated gust fronts (i.e. arc clouds), highlights relative minima and maxima of radial outflow and inflow during different times

of day, and indicates enhanced vertical winds at the location of the squall line. Key findings from the NRH1 analyses reveal the following:

1. *OLR and upper-level ice mixing ratio*: OLR analyses show a distinct diurnal oscillation that appears to propagate away from the storm each day at speeds of approximately 5-10  $\text{m s}^{-1}$ , beginning at  $R \sim 150$  km and eventually reaching  $R \sim 450$  km. Peak OLR cooling occurs from  $\sim 0600$ - $1800$  LST and has similar timing to previously discovered radially propagating diurnal pulses that have been detected in infrared satellite imagery by Dunion et al. (2014). Complimentary analyses of ice mixing ratio at  $\sim 200$  hPa suggest that a distinct radially propagating diurnal signal is present in the upper-level outflow layer of the storm.
2. *Temperature and moisture*: analyses of potential temperature reveal a TCDC signal (especially at radii of  $\geq 150$  km) that involves a relatively deep layer of the storm and its surrounding environment. Examination of mixing ratio indicates a propagating diurnal signal that is particularly pronounced near the TC outflow layer and at lower levels ( $\sim 925$  hPa to the near surface). The upper-level trends are similar to those seen on OLR, ice mixing ratio, and potential temperature, suggesting that diurnal pulses are characterized by marked changes in both temperature and moisture. Diurnal oscillations in low-level (e.g. 925 hPa to the near surface) moisture appear to manifest as periodic minima that are concentrated at  $R \sim 100$ - $300$  km, extend from  $z \sim 4$  km to the surface, and may be linked to large arc cloud features that form along the leading edge of TC diurnal pulses. This suggests that TCDC moisture signals may behave like squall line features with associated outflow boundaries that propagate away from the NRH1 storm each day.

3. *Radiation, LNB and CAPE*: Middle to upper-level ( $z \sim 4\text{-}12$  km) diurnal fluctuations of shortwave and longwave radiation in the TC inner core and surrounding environment appear to have profound effects on the LNB and hence, CAPE in the storm each day. Although shortwave and longwave radiation tendencies consistently support very low CAPE ( $\sim 0\text{-}500$  J kg<sup>-1</sup>) inside the TC inner core ( $R \sim \leq 150$  km), the region just outside the inner core ( $R \sim 150\text{-}350$  km) experiences marked diurnal fluctuations of the LNB and CAPE. These parameters fluctuate by as much as 450 hPa and 1500 J kg<sup>-1</sup> respectively and favor a convectively primed (i.e. more convectively favorable) environment in the late evening to early morning hours in this region of the storm. This nighttime enhancement of CAPE at  $R \sim 150\text{-}350$  km could favor the formation of convectively active TC diurnal pulses at this radius range and could partly explain why TC diurnal pulses as seen in both satellite imagery and the NRH1 appear to form at  $R \sim 150$  km after sunset each day.
4. *10-m Surface Winds*: 10-m surface winds showed a clear diurnal signal and indicated that there are marked periods of alternated enhanced (evening to early morning hours) and suppressed (mid-morning to afternoon hours) surface winds and low-level inflow each day, particularly along the periphery and just outside the storm's inner core ( $R \sim 100\text{-}350$  km). These findings suggest that the TCDC has implications for forecasting TC intensity and structure (e.g. radii of 34 and 50 kt winds). These aspects of the TCDC will be investigated in future work.
5. *Radial winds*: Radial winds in the NRH1 show significant diurnal oscillations near the level of the outflow layer with regular outward bursts evident at  $R \sim 150$  km in the morning hours each day that steadily propagate out to peripheral radii (e.g.  $R = 450$  km) during the afternoon. These outflow maxima are interrupted by lulls in outflow that peak in the late

evening and are a factor of two weaker than the periods of maximum outflow. Middle level (e.g. 700 hPa) radial wind also has a diurnal inflow peak in the mid- morning and appears to occur prior to and radially outward of the aforementioned upper-level outflow bursts. These diurnal patterns of middle level inflow suggest that the morning could be a time when the TC is more susceptible to middle level ventilation. Low-level (~925 hPa to the surface) radial winds in the NRH1 also indicated that peak inflow at R~100-200 km occurs in the early morning hours and is interspersed by periods of relatively weaker inflow that are weakest in the late morning to afternoon.

6. *Tangential Winds*: Diurnal patterns of tangential wind exhibit marked diurnal signals throughout the troposphere and are most pronounced in the upper-levels (e.g. 200 hPa). Peaks in upper-level tangential wind occur from the mid-afternoon to early evening at R~300-450 km and are interspersed by lulls that are 1.5-5 times weaker.
7. *Vertical Winds*: the NRH1 exhibits a clear diurnal signal of vertical winds near the level of the TC outflow layer (~200 hPa), but in the mean, these diurnal signals are less defined in the lower (e.g. 925 hPa to the near-surface) and especially middle (e.g. 700 hPa) levels. Two-dimensional plots of vertical wind made during several of the days of NRH1 peak intensity reveal narrow (~10-20 km wide), highly symmetric rings of enhanced vertical winds that propagate away from the storm each day. These rings of enhanced vertical winds appear to involve a deep layer of the troposphere and the timing of their propagation closely matches the TCDC conceptual clock presented by Dunion et al. (2014). These features are also similar in appearance to the 37 and 85 GHz microwave convective rings (i.e. diurnal pulses) that were described in that work and may be a signature of the diurnal pulse.

8. *Precipitation*: Analyses of NRH1 rain rates and simulated radar reflectivity showed a strong outwardly propagating diurnal signal. Maxima (minima) in precipitation peak in the late evening to early morning (late morning to middle afternoon) in the inner core and in the early to late morning (late afternoon to late evening) farther from the storm (e.g.  $R=200-450$  km). These trends suggest that the TCDC may have implications for quantitative precipitation forecasting and TC structure. Analyses of Q-condensate and vertical wind suggested that TC diurnal pulses might behave like squall lines that are accompanied by outflow boundaries (i.e. arc clouds).

The two schematics that are presented (Figs. 26 and 27) summarize many of the main findings in this work. The first schematic describes the basic state of the TC environment as the TCDC evolves during its early and later stages each day, while the second describes the TCDC-centric daytime evolution of a TC diurnal pulse, associated squall lines and gust fronts, and radial and vertical winds in the lower and upper levels of the storm. It is hypothesized that enhanced nighttime radiational cooling that is particularly favored in the TC outflow layer (relative to surrounding cloud-free air) may act to prime (i.e. pre-condition) the TC environment in a way that favors triggering of the TCDC via the mechanisms described by Dunion et al. 2014 (e.g. convectively-driven gravity waves, radiatively reduced outflow resistance, cloud-cloud-free differential heating, seeder-feeder mechanism, or some combination of these mechanisms). During the daytime, the stabilizing effects of shortwave warming suppress TCDC process in the storm environment, which leads to the culmination of TCDC each day. If the TCDC and associated TC diurnal pulses are indeed found to be linked to gravity wave features, as suggested by Dunion

et al. 2014, the latter term may be better described as a TC diurnal wave. This will be the topic of future work.

The NRH1 that was examined here indicates robust TCDC signals in radiation, thermodynamics, static stability, winds, and precipitation. Since the NRH1 was created using the Weather Research and Forecasting (WRF) model, the TCDC signals highlighted here have implications on a wide-range of research studies that have utilized this model, as well as NOAA's operational Hurricane Weather Research and Forecast System (HWRF) model that is a version of the WRF Nonhydrostatic Mesoscale Model (NMM) tailored for tropical cyclone forecasting. Identifying TCDC signals in models like WRF and HWRF offers opportunities to both further our understanding of TCDC processes and to understand how the TCDC affects the representation, analyses, and forecasts of TCs in numerical simulations. Future work will continue to integrate satellite data, numerical model simulations, and observations of the TCDC with a goal of continued advancement of our understanding of this possibly fundamental TC process.

## **Acknowledgements**

The authors would like to thank John Molinari, Ryan Torn, Lance Bosart, Frank Marks, and Chris Velden (aka the “hive”) for their many insightful discussions related to the TC diurnal cycle and this work. This paper benefited from reviews by Rob Rogers from the NOAA/AOML/Hurricane Research Division and Altug Aksoy from the University of Miami/CIMAS-NOAA/AOML/Hurricane Research Division.

## References

- Aberson, S.D., 2010: 10 years of hurricane synoptic surveillance (1997–2006), *Mon. Wea. Rev.*, **138**, 1536-1549.
- Aksoy, A., 2013: Storm-relative observations in tropical cyclone data assimilation with an Ensemble Kalman Filter, *Mon. Wea. Rev.*, **141**, 506-522.
- Bergeron, T., 1935: On the physics of cloud and precipitation. *Proc. 5th Assembly U.G.G.I. Lisbon*, **Vol. 2**, p. 156.
- Browner, S. P., W. L. Woodley, and C. G. Griffith, 1977: Diurnal oscillation of cloudiness associated with tropical storms. *Mon. Wea. Rev.*, **105**, 856–864.
- Bryan, G. H., and M.D. Parker, 2010: Observations of a squall line and its near environment using high-frequency rawinsonde launches during VORTEX2. *Mon. Wea. Rev.*, **138**, 4076-4097.
- Bu, Y.P., R.G. Fovell, and K.L. Corbosiero, 2014: Influence of cloud–radiative forcing on tropical cyclone structure. *J. Atm. Sci.*, **71**, 1644-1662.
- Chen, S., and W.R. Cotton, 1988: The sensitivity of a simulated extratropical mesoscale convective system to longwave radiation and ice-phase microphysics. *J. Atm. Sci.*, **45**, 3897-3910.
- Cotton, W.R., G. Bryan, and S.C. Van Den Heever, 2010: Storm and Cloud Dynamics. Academic Press 809 pp.
- Crook, N.A., 1988: Trapping of internal low-level internal gravity waves. *J. Atmos. Sci.*, **45**, 1533-1541.
- DeMaria, M., M. Mainelli, L.K. Shay, J.A. Knaff, and J. Kaplan, 2005: Further improvement to the Statistical Hurricane Intensity Prediction Scheme (SHIPS). *Wea. Forecasting*, **20:4**, 531-543.

- Demuth, J., M. DeMaria, and J. A. Knaff, 2006: Improvement of advanced microwave sounder unit tropical cyclone intensity and size estimation algorithms. *J. Appl. Meteor. Climatol.*, **45**, 1573–1581.
- Dunion, J.P., C.D. Thorncroft, and C.S. Velden, 2014: The tropical cyclone diurnal cycle of mature hurricanes. *Mon. Wea. Rev.*, **142**, 3900-3919.
- Dunion, J. P., 2011: Rewriting the climatology of the tropical North Atlantic and Caribbean Sea atmosphere. *J. Climate*, **24**, 893-908.
- Duran, P., and J. Molinari, 2016: Upper-tropospheric low Richardson number in tropical cyclones: sensitivity to cyclone intensity and the diurnal cycle. *J. Atmos. Sci.*, **73**, 545-554.
- Gallina, G.M., and C.S. Velden, 2000: A quantitative look at the relationship between environmental vertical wind shear and tropical cyclone intensity change utilizing enhanced satellite derived wind information. Preprints, *24th Conf. on Hurricanes and Tropical Meteorology*, Ft. Lauderdale, FL, Amer. Meteor. Soc., 7A.4. [Available online at <https://ams.confex.com/ams/last2000/webprogram/24HURRICANES.html>.]
- Gray, W. M., and R. W. Jacobson, 1977: Diurnal variation of deep cumulus convection. *Mon. Wea. Rev.*, **105**, 1171–1188.
- Hawkins, J. D., and C. Velden, 2011: Supporting meteorological field experiment missions and post-mission analysis with satellite digital data and products. *Bull. Amer. Meteor. Soc.*, **92**, 1009–1022.
- Hawkins, J. D., T.F. Lee, K. Richardson, C. Sampson, F. J. Turk, and J. E. Kent, 2001: Satellite multisensor tropical cyclone structure monitoring. *Bull. Amer. Meteor. Soc.*, **82**, 567–578.
- Hayden, C. M., and R. Purser, 1995: Recursive Filter Objective Analysis of Meteorological Fields: Applications to NESDIS Operational Processing. *J. Appl. Meteor.*, **34**, 3-15.

- Hock, T.F., and J.F. Franklin, 1999: The NCAR GPS dropwindsonde. *Bull. Amer. Meteor. Soc.*, **80**, 407-420.
- Holmlund, K., C. Velden, and M. Rohn, 2001: Enhanced Automated Quality Control Applied to High-Density Satellite-Derived Winds. *Mon. Wea. Rev.*, **129**, 517-529.
- Hong, S.-Y., Y. Noh, and J. Dudhia, 2006: A new vertical diffusion package with an explicit treatment of entrainment processes, *Mon. Wea. Rev.*, **134**, 2318–2341.
- Houze, R.A., S.A. Rutledge, T.J. Matejka, and P. V. Hobbs, 1981: The mesoscale and microscale structure and organization of clouds and precipitation in midlatitude cyclones. III: air motions and precipitation growth in a warm-frontal rainband. *J. Atmos. Sci.*, **38**, 639-649.
- Iacono, M. J., J. S. Delamere, E. J. Mlawer, M. W. Shephard, S. A. Clough, and W. D. Collins, 2008: Radiative forcing by long-lived greenhouse gases: Calculations with the AER radiative transfer models, *J. Geophys. Res.*, **113**, D13103.
- Jarvinen, B. R., C. J. Neumann, and M. A. S. Davis, 1984: A tropical cyclone data tape for the North Atlantic basin, 1886-1983: Contents, limitations, and uses. NOAA Tech. Memo. NWS NHC 22, 21 pp.
- Kain, J. S., and J. M. Fritsch, 1990: A one-dimensional entraining/detraining plume model and its application in convective parameterization, *J. Atmos. Sci.*, **47**, 2418–2436.
- Knaff, J. A., S. P. Longmore, D. A. Molnar, 2014: An objective satellite-based tropical cyclone size climatology. *J. Climate*, **27**, 455–476.
- Knaff, J.A., and J. F. Weaver, 2000: A mesoscale low-level thunderstorm outflow boundary associated with Hurricane Luis. *Mon. Wea. Rev.*, **128**, 3352–3355.

- Kossin, J.P., J.A. Knaff, H.I. Berger, D.C. Herndon, T.A. Cram, C.S. Velden, R.J. Murnane, and J.D. Hawkins, 2007: Estimating hurricane wind structure in the absence of aircraft reconnaissance. *Wea. Forecasting*, **22**:1, 89–101.
- Kossin, J. P., 2002: Daily hurricane variability inferred from GOES infrared imagery. *Mon. Wea. Rev.*, **130**, 2260–2270.
- Kraus, E.B., 1963: The diurnal precipitation change over the sea. *J. Atm. Sci.*, **20**, 546-551.
- Lazzara, M. A., and Coauthors, 1999: The Man computer Interactive Data Access System: 25 Years of Interactive Processing. *Bull. Amer. Meteor. Soc.*, **80**, 271–284.
- Lee, C. S., K. K. W. Cheung, W.-T. Fang, and R. L. Elsberry, 2010: Initial maintenance of tropical cyclone size in the western North Pacific. *Mon. Wea. Rev.*, **138**, 3207-3223.
- Lee, T. F., F. J. Turk, J. D. Hawkins, and K. A. Richardson, 2002: Interpretation of TRMM TMI images of tropical cyclones, *Earth Interact.*, **6**, 3.
- Lim, K.-S. S., and S.-Y. Hong, 2010: Development of an effective double-moment cloud microphysics scheme with prognostic cloud- condensation nuclei (CCN) for weather and climate models, *Mon. Weather Rev.*, **138**, 1587–1612.
- Liu, C., and M. W. Moncrieff, 1998: A numerical study of the diurnal cycle of tropical oceanic convection. *J. Atmos. Sci.*, **55**, 2329–2344.
- Mapes, B. E., and R.A. Houze Jr., 1993: Cloud clusters and super- clusters over the oceanic warm pool. *Mon. Wea. Rev.*, **121**, 1398–1415.
- Marks, F.D., 1985: Evolution and structure of precipitation in Hurricane Allen (1980). *Mon. Wea. Rev.* **113**, 909-930.
- Martin, D.W., 1975: Characteristics of West Africa and Atlantic cloud clusters. GATE Rep. No. **14**, Preliminary Scientific Results, Vol. **1**, 182-190.

- Mecikalski, J.R., and G.J. Tripoli, 1998: Inertial Available Kinetic Energy and the dynamics of tropical plume formation. *Mon. Wea. Rev.*, **126**, 2200–2216.
- Metcalf, J., 1975: Gravity waves in a low-level inversion. *J. Atmos. Sci.*, **32**, 351-361.
- Molinari, J., P. Duran, and D. Vollaro, 2014: Low Richardson number in the tropical cyclone outflow layer. *J. Atmos. Sci.*, **71**, 3164-3179.
- Mueller, K.J., M. DeMaria, J.A. Knaff, J.P. Kossin, T.H. Vonder Haar, 2006: Objective estimation of tropical cyclone wind structure from infrared satellite data. *Wea. Forecasting*, **21**:6, 990–1005.
- Nappo, C.J., 2013: *An Introduction to Atmospheric Gravity Waves*. Academic Press, 359 pp.
- Navarro, E.L., and G.J. Hakim, 2016: Idealized numerical modeling of the diurnal cycle of tropical cyclones. *J. Atmos. Sci.*, **73**, 4189-4201.
- Noh, Y., W. G. Cheon, S. Y. Hong, and S. Raasch, 2003: Improvement of the K-profile model for the planetary boundary layer based on large eddy simulation data, *Boundary Layer Meteorol.*, **107**, 421–427.
- Nolan, D. S., R. M. Atlas, K. T. Bhatia, and L. R. Bucci, 2013: Development and validation of a hurricane nature run using the joint OSSE nature run and WRF model. *J. Adv. Model. Earth Syst.*, **5**, 382–405.
- Olander, T. L., and C. S. Velden, 2007: The Advanced Dvorak Technique: Continued development of an objective scheme to estimate tropical cyclone intensity using geostationary infrared satellite imagery. *Wea. Forecasting*, **22**, 287–298.
- Pfister, L., K.R. Chan, T.P. Bui, S. Bowen, M. Legg, B. Gary, K. Kelly, M. Proffitt, and W Starr, 1993: Gravity waves generated by a tropical cyclone during the STEP tropical field program. *J. Geophys. Res.*, **98**, 273-8638.

- Randall, D.A., Harshvardhan, and D.A. Dazlich, 1991: Diurnal variability of the hydrologic cycle in a general circulation model. *J. Atmos. Sci.*, **48**, 40-62.
- Rogers, R. F., S. Lorsolo, P. Reasor, J. Gamache, and F. Marks, 2012: Multiscale analysis of tropical cyclone kinematic structure from airborne Doppler radar composites. *Mon. Wea. Rev.*, **140**, 77–99.
- Tang, B., and K. Emanuel, 2012: A ventilation index for tropical cyclones. *Bull. Amer. Meteor. Soc.*, **93**, 1901-1912.
- Tang, X, and F. Zhang, 2016: Impacts of the diurnal radiation cycle on the formation, intensity, and structure of Hurricane Edouard (2014). *J. Atmos. Sci.*, **73**, 2871-2892.
- Tripoli, G. J., and W.R. Cotton, 1989: Numerical study of an observed orogenic mesoscale convective system. Part 1: Simulated genesis and comparison with observations. *Mon. Wea. Rev.*, **117**, 273-304.
- Velden, C.S., B. Harper, F. Wells, J.L. Beven II, R. Zehr, T. Olander, M. Mayfield, C. Guard, M. Lander, R. Edson, L. Avila, A. Burton, M. Turk, A. Kikuchi, A. Christian, P. Caroff, P. McCrone, 2006: The Dvorak tropical cyclone intensity estimation technique: A satellite-based method that has endured for over 30 years. *Bull. Amer. Meteor. Soc.*, **87**, 1195-1210.
- Velden, C. S., C. Hayden, S. Nieman, W. Menzel, S. Wanzong, and J. Goerss, 1997: Upper-Tropospheric Winds Derived from Geostationary Satellite Water Vapor Observations. *Bull. Amer. Meteor. Soc.*, **78**, 173-195.
- Weickmann, H. K., A. B. Long, and L. R. Hoxit, 1977: Some examples of rapidly growing oceanic cumulonimbus clouds. *Mon. Wea. Rev.*, **105**, 469–476.

- Willoughby, H.E., J.A. Clos, and M.G. Shoreibah, 1982: Concentric eye walls, secondary wind maxima, and the evolution of the hurricane vortex. *J. Atmos. Sci.*, **39**, 395-411.
- Yang, G., and J. Slingo, 2001: The diurnal cycle in the tropics. *Mon. Wea. Rev.*, **129**, 784–801.
- Zipser, E. J., 1977: Mesoscale and convective–scale downdrafts as distinct components of squall line structure. *Mon. Wea. Rev.*, **105**, 1568–1589.

## List of Figures

1. 3-hourly (a) track, (b) minimum surface pressure, and (c) maximum 10-m wind speed for the 13-day NRH1 simulation. The light blue line in (c) denotes the Saffir-Simpson category 2 wind speed threshold ( $43 \text{ m s}^{-1}$ ).
2. Hovmollers of azimuthally averaged OLR ( $\text{W m s}^{-2}$ ) calculated for (left) the period from 29 Aug-08 August of the NRH1 and (right) only for the 03-08 August NRH1 study period. Radii are analyzed relative to the TC center and extend out to 450 km.
3. Hovmollers of azimuthally averaged shortwave, longwave, and total radiation tendencies ( $\text{K h}^{-1}$ ) derived from the NRH1. Analyses are derived over the 03-08 August study period and show the 200, 700, and 925 hPa pressure levels. Radii are analyzed relative to the TC center and extend out to 450 km.
4. Hovmoller of azimuthally averaged ice mixing ratio ( $\text{g kg}^{-1}$ ) derived from the 03-08 August NRH1 study period for 200 hPa (top). Radius-height cross-sections of azimuthally averaged ice mixing ratio derived from the NRH1 on (A) 06 Aug 0100 UTC (2100 LST) and (B) 06 Aug 1600 UTC (1200 LST) are also shown. The white dashed lines indicated the times along the Hovmoller plot when both cross-sections were derived. Radii in all plots are analyzed relative to the TC center and extend out to 450 km.

5. 200 hPa azimuthally averaged (top) ice mixing ratio ( $\text{g kg}^{-1}$ ) and longwave radiation tendency ( $\text{K h}^{-1}$ ) derived from the 03-08 August NRH1 study period at 300 and 400 km radii.
  
6. 3-hourly radius-height cross-sections of azimuthally averaged total radiation tendency ( $\text{K h}^{-1}$ ) derived from the NRH1 from 06 Aug 0000 LST to 07 Aug 0000 LST. The shaded boxes highlight the regions from  $z=3-13$  km from  $R=50-200$  km (A) and  $R=200-400$  km (B). The bold contours denote regions of zero net radiation tendencies. Radii are analyzed relative to the TC center and extend out to  $R=450$  km.
  
7. 3-hourly radius-height cross-sections of azimuthally averaged shortwave radiation tendency ( $\text{K h}^{-1}$ ) derived from the NRH1 from 06 Aug 0000 LST to 07 Aug 0000 LST. The shaded boxes highlight the regions from  $z=3-13$  km from  $R=50-200$  km (A) and  $R=200-400$  km (B). The bold contours denote regions of zero net radiation tendencies. Radii are analyzed relative to the TC center and extend out to  $R=450$  km.
  
8. 3-hourly radius-height cross-sections of azimuthally averaged longwave radiation tendency ( $\text{K h}^{-1}$ ) derived from the NRH1 from 06 Aug 0000 LST to 07 Aug 0000 LST. The shaded boxes highlight the regions from  $z=3-13$  km from  $R=50-200$  km (A) and  $R=200-400$  km (B). The bold contours denote regions of zero net radiation tendencies. Radii are analyzed relative to the TC center and extend out to  $R=450$  km.

9. Hovmollers of azimuthally averaged potential temperature (K) derived from the 03-08 August NRH1 study period for 200 hPa, 700 hPa, 925 hPa, and 40 m. Radii are analyzed relative to the TC center and extend out to 450 km.
10. Azimuthally averaged potential temperature (K) derived from the 03-08 August NRH1 study period for the 200 hPa, 700 hPa, 925 hPa, and 40 m vertical levels. Analyses include the 150, 300, and 450 km radii.
11. Hovmollers of azimuthally averaged mixing ratio ( $\text{g kg}^{-1}$ ) derived from the 03-08 August NRH1 study period for 200 hPa, 700 hPa, 925 hPa, and 40 m. Radii are analyzed relative to the TC center and extend out to 450 km.
12. Azimuthally averaged mixing ratio ( $\text{g kg}^{-1}$ ) derived from the 03-08 August NRH1 study period for the 200 hPa, 700 hPa, 925 hPa, and 40 m vertical levels. Analyses include the 150, 300, and 450 km radii.
13. Hovmoller of azimuthally averaged CAPE ( $\text{J kg}^{-1}$ ) derived from the 03-08 August NRH1 study period. Radii are analyzed relative to the TC center and extend out to  $R=450$  km.
14. Azimuthally averaged CAPE (top) and the level of neutral buoyancy (LNB) derived from the 03-08 August NRH1 study period at the 150, 200, and 300 km radii.

15. CAPE ( $\text{J kg}^{-1}$ ) derived from the NRH1 for 06-07 August. Images are 3-hourly from 06 Aug 0200 LST (0600 UTC) to 07 Aug 0200 LST (0600 UTC).
16. Hovmollers of azimuthally averaged 10-m surface winds ( $\text{m s}^{-1}$ ) derived from the 03-08 August NRH1 study period for (a) wind speed, (b) radial wind speed, and (c) tangential wind speed. Radii are analyzed relative to the TC center and extend out to  $R=450$  km.
17. Plots of azimuthally averaged 10-m surface winds ( $\text{m s}^{-1}$ ) derived from the 03-08 August NRH1 study period for 50, 100, 150, and 200 km radii.
18. Hovmollers of azimuthally averaged radial wind ( $\text{m s}^{-1}$ ) derived from the 03-08 August NRH1 study period for 200 hPa, 700 hPa, 925 hPa, and 40 m. Radii are analyzed relative to the TC center and extend out to 450 km.
19. Hovmollers of azimuthally averaged tangential wind ( $\text{m s}^{-1}$ ) derived from the 03-08 August NRH1 study period for 200 hPa, 700 hPa, 925 hPa, and 40 m. Radii are analyzed relative to the TC center and extend out to  $R=450$  km.
20. Hovmollers of azimuthally averaged vertical wind ( $\text{m s}^{-1}$ ) derived from the 03-08 August NRH1 study period for 200 hPa, 700 hPa, 925 hPa, and 40 m. Radii are analyzed relative to the TC center and extend out to 450 km.

21. Plots of vertical wind ( $\text{m s}^{-1}$ ) derived from the NRH1 from 0200-1400 LST (0600-1800 UTC) on 06 August at 200 hPa, 700, and 925 hPa. A relatively deep layer semi-circular feature is indicated 200-300 km outside of the eyewall that has  $1\text{-}3 \text{ m s}^{-1}$  vertical motion and is propagating away from the TC.
22. Hovmoller of rain rate ( $\text{mm h}^{-1}$ ) derived from the 03-08 August NRH1 study period. Radius is analyzed relative to the TC center and extends out to  $R=450 \text{ km}$ .
23. Plots of azimuthally averaged rain rate ( $\text{mm hr}^{-1}$ ) derived from the 03-08 August NRH1 study period at the 100, 150, 200, and 250 km radii.
24. Hovmollers of simulated radar reflectivity (dBZ) derived from the 03-08 August NRH1 study period for 200 hPa, 700 hPa, 925 hPa, and 40 m. Radii are analyzed relative to the TC center and extend out to  $R=450 \text{ km}$ .
25. 6-hourly radius-height plots of Q-condensate from the NRH1 on 06 August from 0000-1800 LST (0400-2200 UTC). Dashed black, solid black, and magenta contours indicate azimuthal mean vertical winds of  $-0.25 \text{ ms}^{-1}$ ,  $+0.25 \text{ ms}^{-1}$ , and  $+0.5 \text{ ms}^{-1}$  respectively.
26. Schematic showing a TC in the (top) initial (i.e. nighttime) and (bottom) later (i.e. daytime) stages of the TCDC. The cross sections show background state parameters of total radiation tendency (Rad Tend,  $\text{K hr}^{-1}$ ),  $\theta$  (K), ice mixing ratio (Ice MR,  $\text{g kg}^{-1}$ ),  $V_r$ -indicated inflow/outflow (inflow/outflow,  $\text{m s}^{-1}$ ), and surface wind speed

(WSpd, m s<sup>-1</sup>) at different levels of the storm. Single level/layer values of OLR (W m<sup>2</sup>), CAPE (J kg<sup>-1</sup>), LNB (height), and rain rate (mm h<sup>-1</sup>) are labeled at the top right of each plot. Red (blue) lettering indicates diurnal maxima (minima) of the various parameters.

27. Schematic showing the evolution of a radially propagating TC diurnal pulse from the early morning to late afternoon. Upper level radial outflow (red arrows), lower level radial inflow (green arrows), and enhanced vertical wind at the location of the TC diurnal pulse (i.e. squall line, blue arrows) are shown. Gust fronts favored to form along the leading edge of the squall line beginning in the mid-morning to late afternoon when it is located at R~300-400 km are shown. Thickness of the radial outflow and inflow lines indicate relative strength at different times of day relative to the position of the squall line. The depth of the squall line is also suggested to lessen as it propagates away from the storm due to a lowering LNB that reaches a minimum in the afternoon.

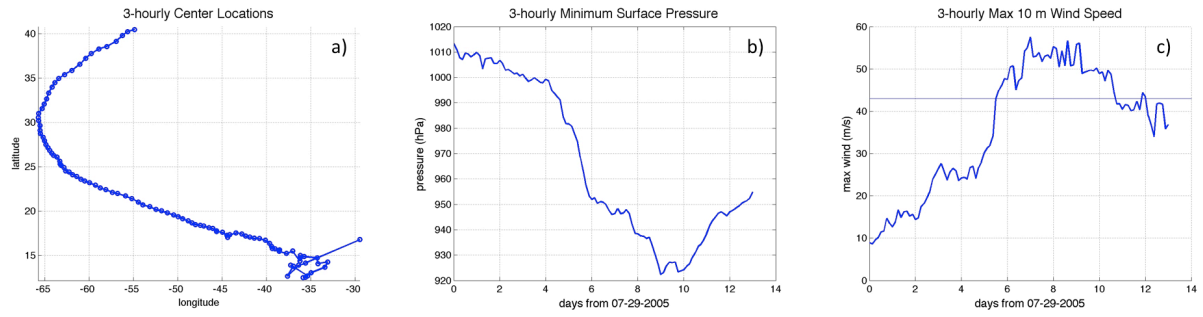


Figure 1: 3-hourly (a) track, (b) minimum surface pressure, and (c) maximum 10-m wind speed for the 13-day NRH1 simulation. The light blue line in (c) denotes the Saffir-Simpson category 2 wind speed threshold ( $43 \text{ m s}^{-1}$ ).

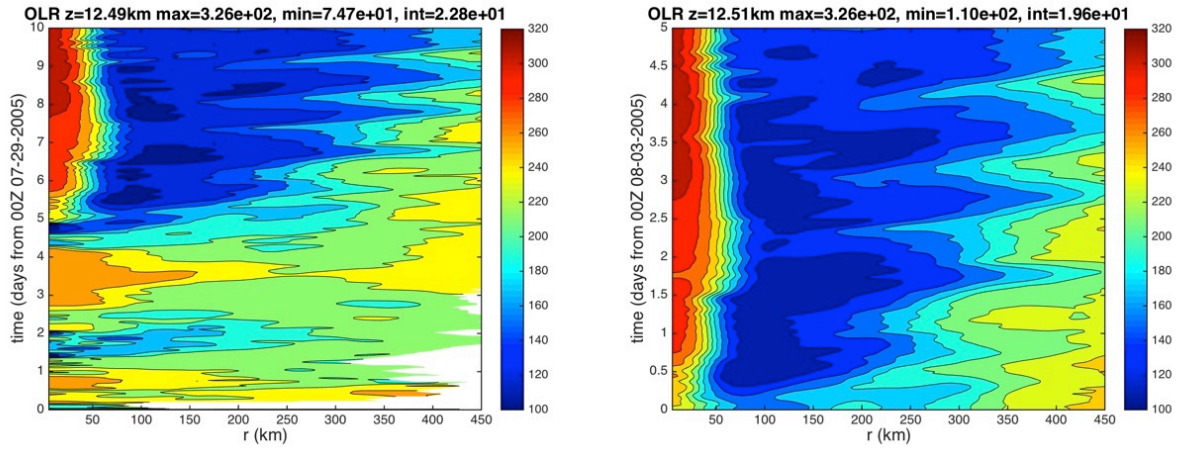


Figure 2: Hovmollers of azimuthally averaged OLR ( $W m s^{-2}$ ) calculated for (left) the period from 29 Aug-08 August of the NRH1 and (right) only for the 03-08 August NRH1 study period. Radii are analyzed relative to the TC center and extend out to 450 km.

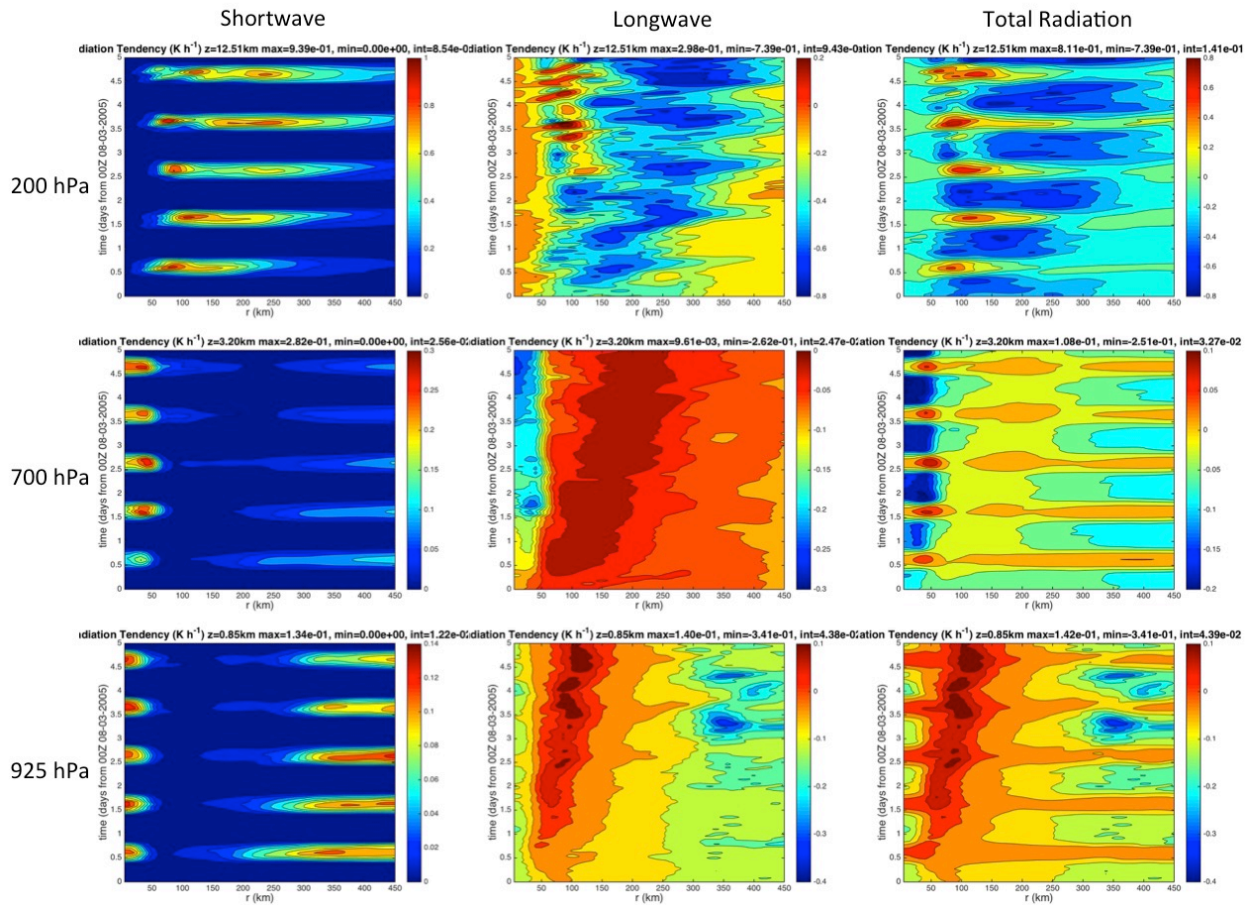


Figure 3: Hovmöller of azimuthally averaged shortwave, longwave, and total radiation tendencies ( $\text{K h}^{-1}$ ) derived from the NRH1. Analyses are derived over the 03-08 August study period and show the 200, 700, and 925 hPa pressure levels. Radii are analyzed relative to the TC center and extend out to 450 km.

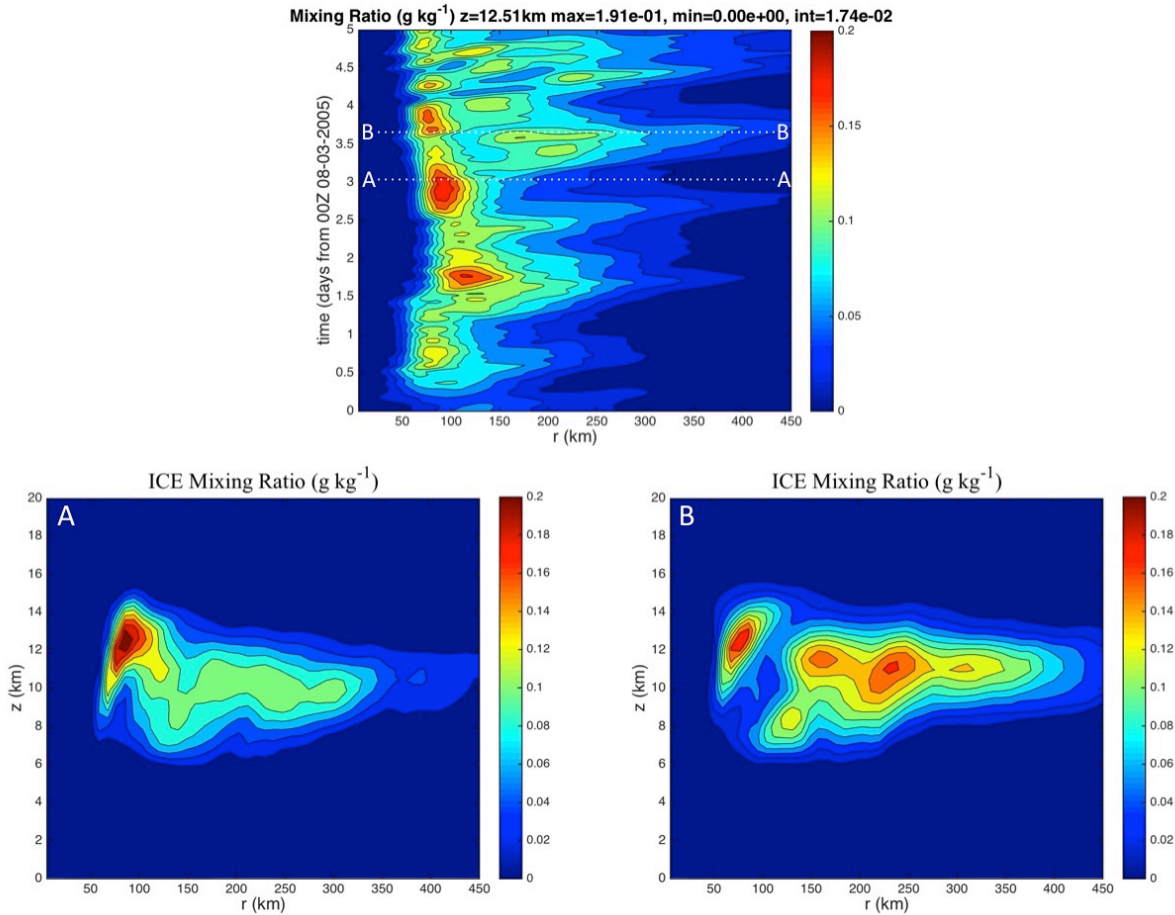


Figure 4: Hovmoller of azimuthally averaged ice mixing ratio ( $\text{g kg}^{-1}$ ) derived from the 03-08 August NRH1 study period for 200 hPa (top). Radius-height cross-sections of azimuthally averaged ice mixing ratio derived from the NRH1 on (A) 06 Aug 0100 UTC (2100 LST) and (B) 06 Aug 1600 UTC (1200 LST) are also shown. The white dashed lines indicated the times along the Hovmoller plot when both cross-sections were derived. Radii in all plots are analyzed relative to the TC center and extend out to 450 km.

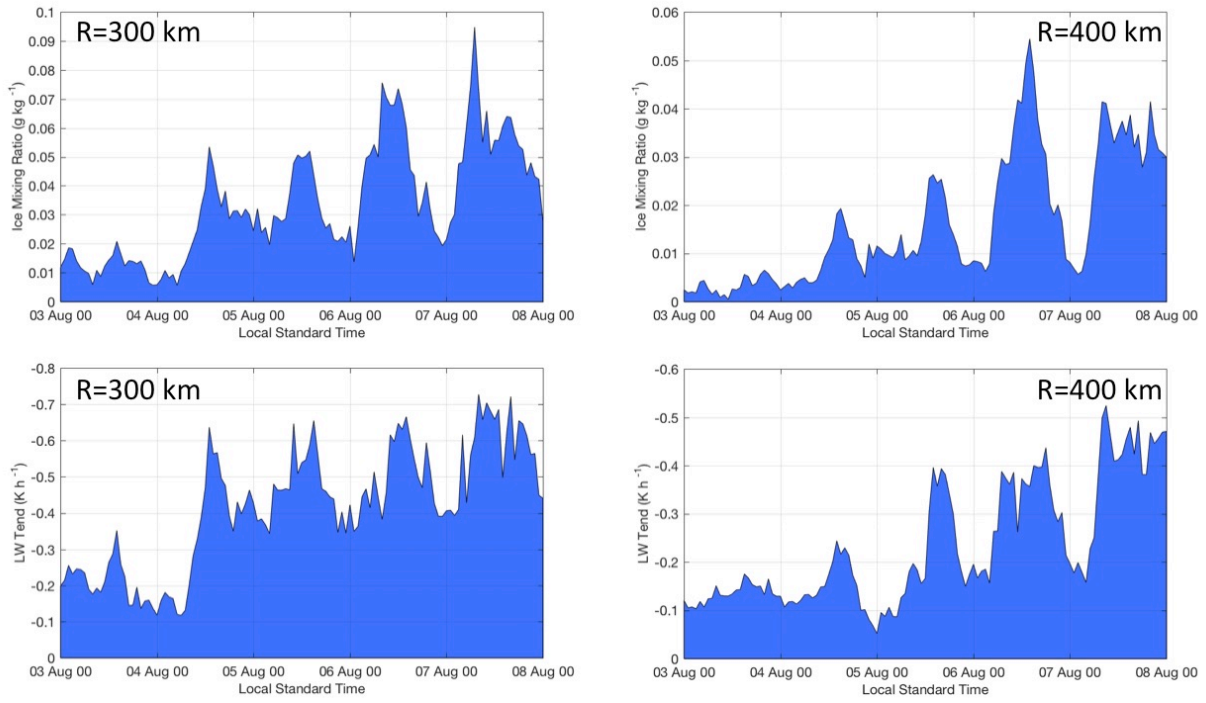


Figure 5: 200 hPa azimuthally averaged (top) ice mixing ratio ( $\text{g kg}^{-1}$ ) and longwave radiation tendency ( $\text{K h}^{-1}$ ) derived from the 03-08 August NRH1 study period at 300 and 400 km radii.

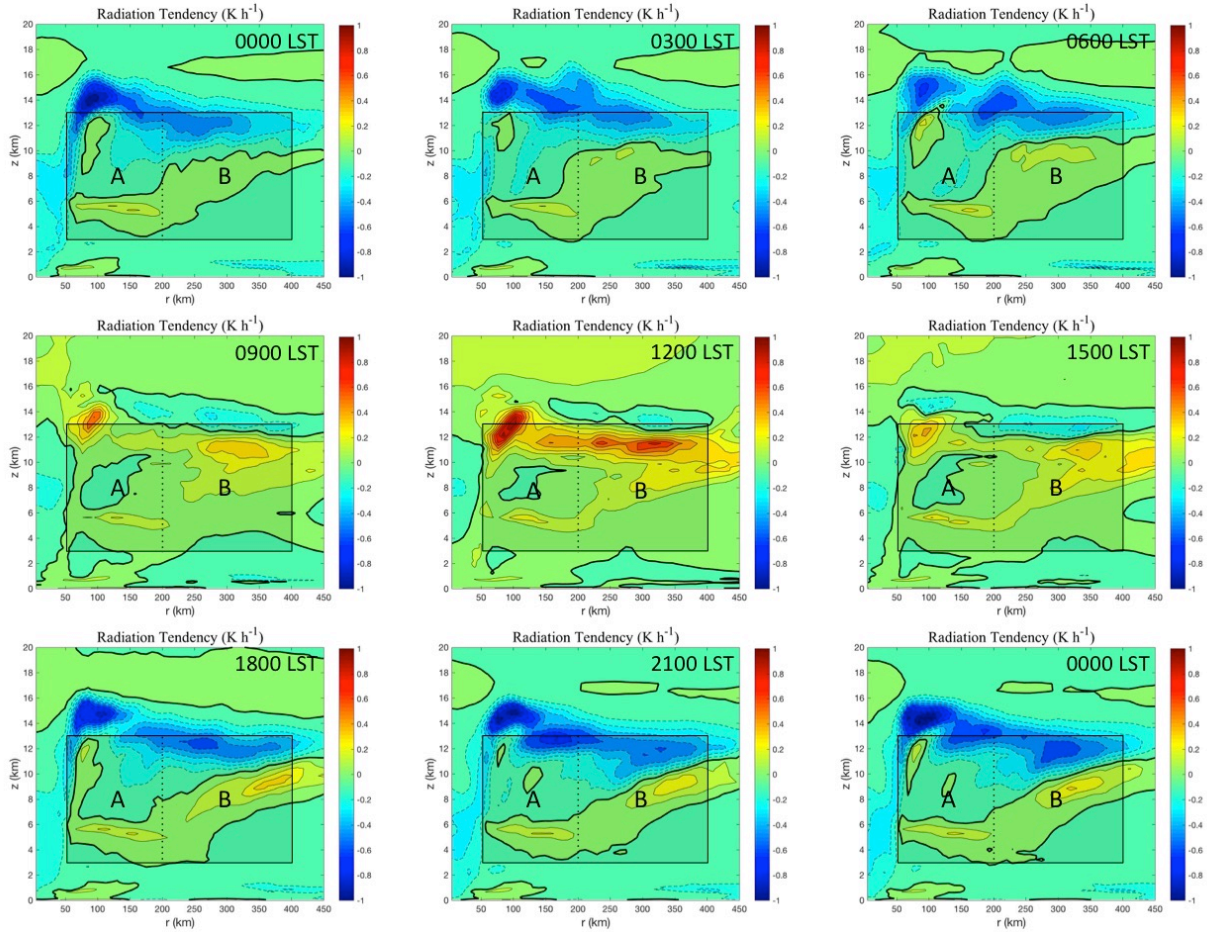


Figure 6: 3-hourly radius-height cross-sections of azimuthally averaged total radiation tendency ( $\text{K h}^{-1}$ ) derived from the NRH1 from 06 Aug 0000 LST to 07 Aug 0000 LST. The shaded boxes highlight the regions from  $z=3\text{-}13$  km from  $R=50\text{-}200$  km (A) and  $R=200\text{-}400$  km (B). The bold contours denote regions of zero net radiation tendencies. Radii are analyzed relative to the TC center and extend out to  $R=450$  km.

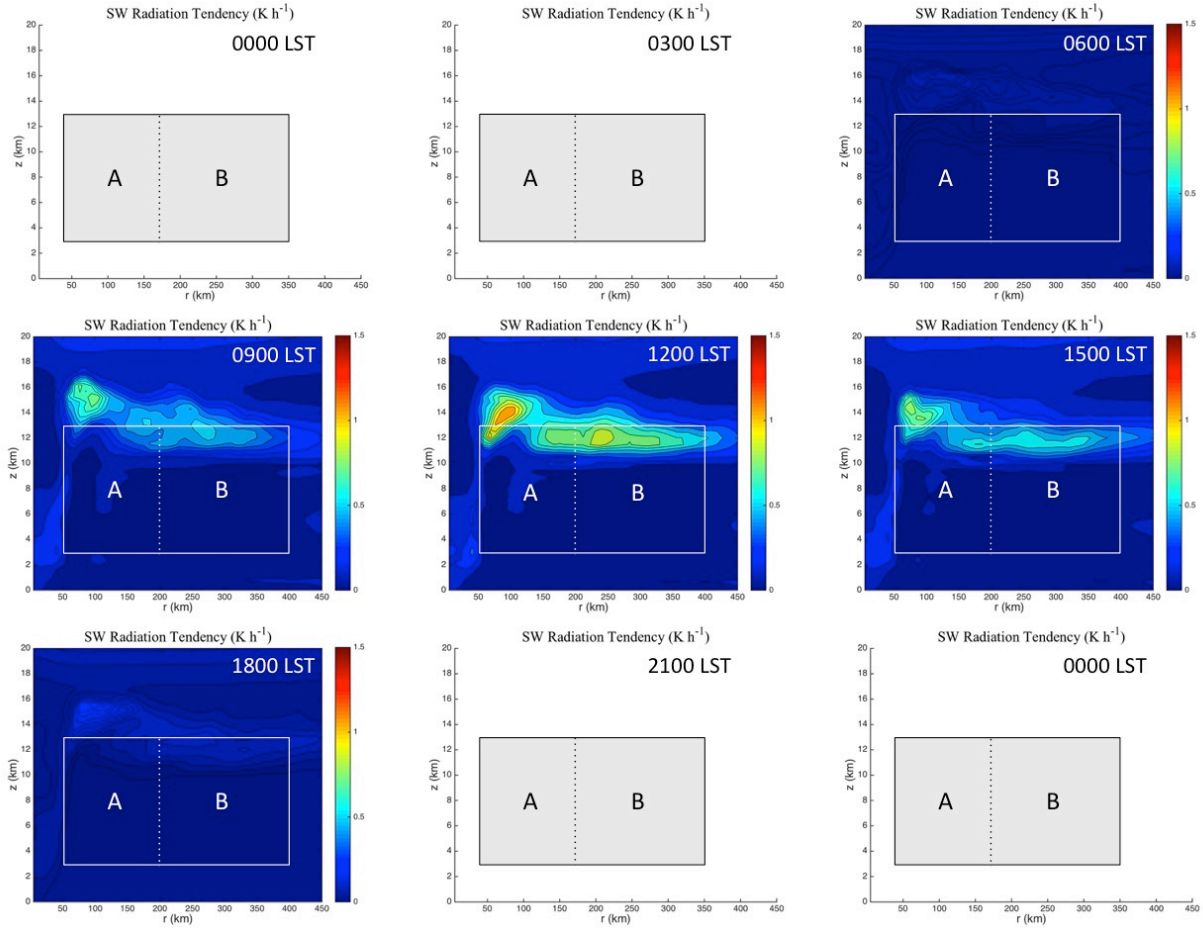


Figure 7: 3-hourly radius-height cross-sections of azimuthally averaged shortwave radiation tendency ( $\text{K h}^{-1}$ ) derived from the NRH1 from 06 Aug 0000 LST to 07 Aug 0000 LST. The shaded boxes highlight the regions from  $z=3\text{-}13$  km from  $R=50\text{-}200$  km (A) and  $R=200\text{-}400$  km (B). The bold contours denote regions of zero net radiation tendencies. Radii are analyzed relative to the TC center and extend out to  $R=450$  km.

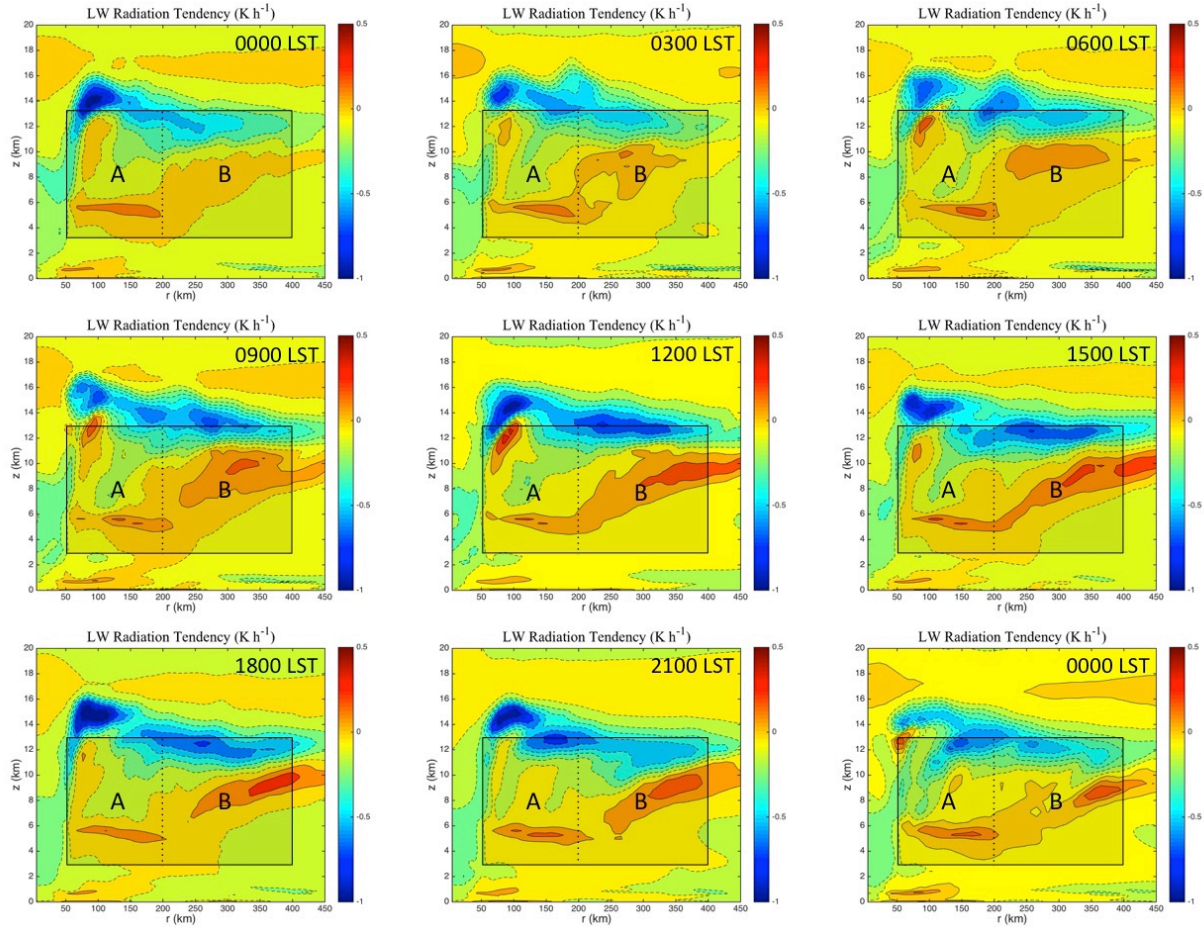


Figure 8: 3-hourly radius-height cross-sections of azimuthally averaged longwave radiation tendency ( $\text{K h}^{-1}$ ) derived from the NRH1 from 06 Aug 0000 LST to 07 Aug 0000 LST. The shaded boxes highlight the regions from  $z=3\text{-}13$  km from  $R=50\text{-}200$  km (A) and  $R=200\text{-}400$  km (B). The bold contours denote regions of zero net radiation tendencies. Radii are analyzed relative to the TC center and extend out to  $R=450$  km.

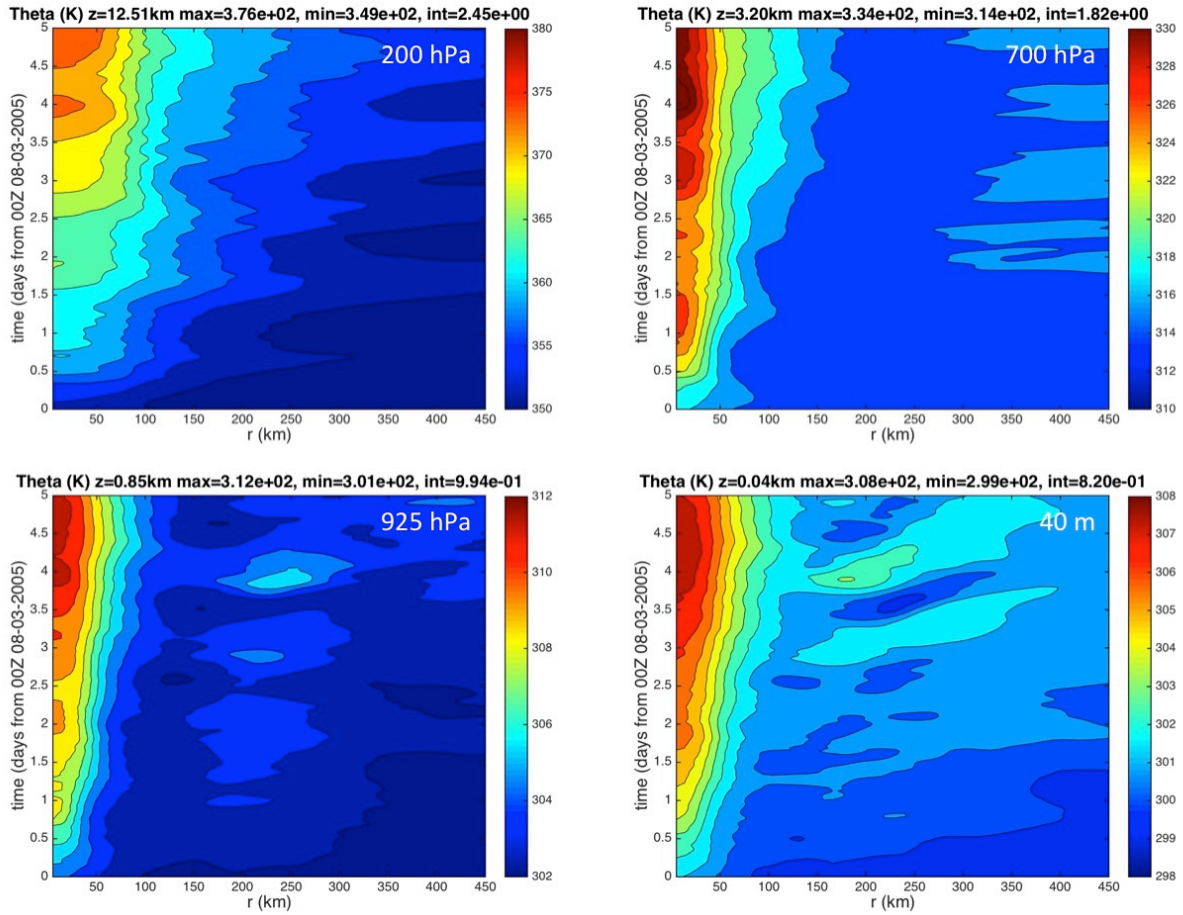


Figure 9: Hovmollers of azimuthally averaged potential temperature (K) derived from the 03-08 August NRH1 study period for 200 hPa, 700 hPa, 925 hPa, and 40 m. Radii are analyzed relative to the TC center and extend out to 450 km.

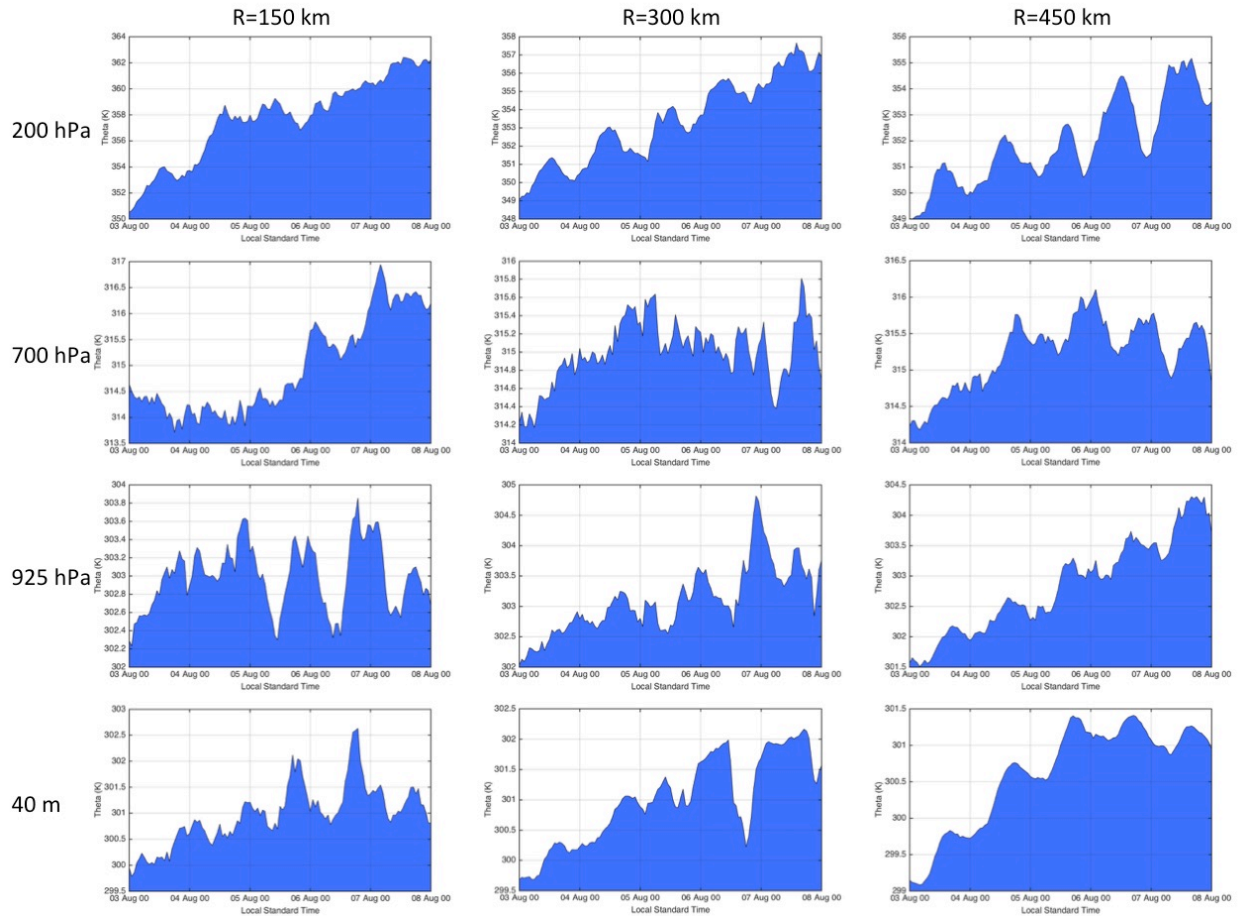


Figure 10: Azimuthally averaged potential temperature (K) derived from the 03-08 August NRH1 study period for the 200 hPa, 700 hPa, 925 hPa, and 40 m vertical levels. Analyses include the 150, 300, and 450 km radii.

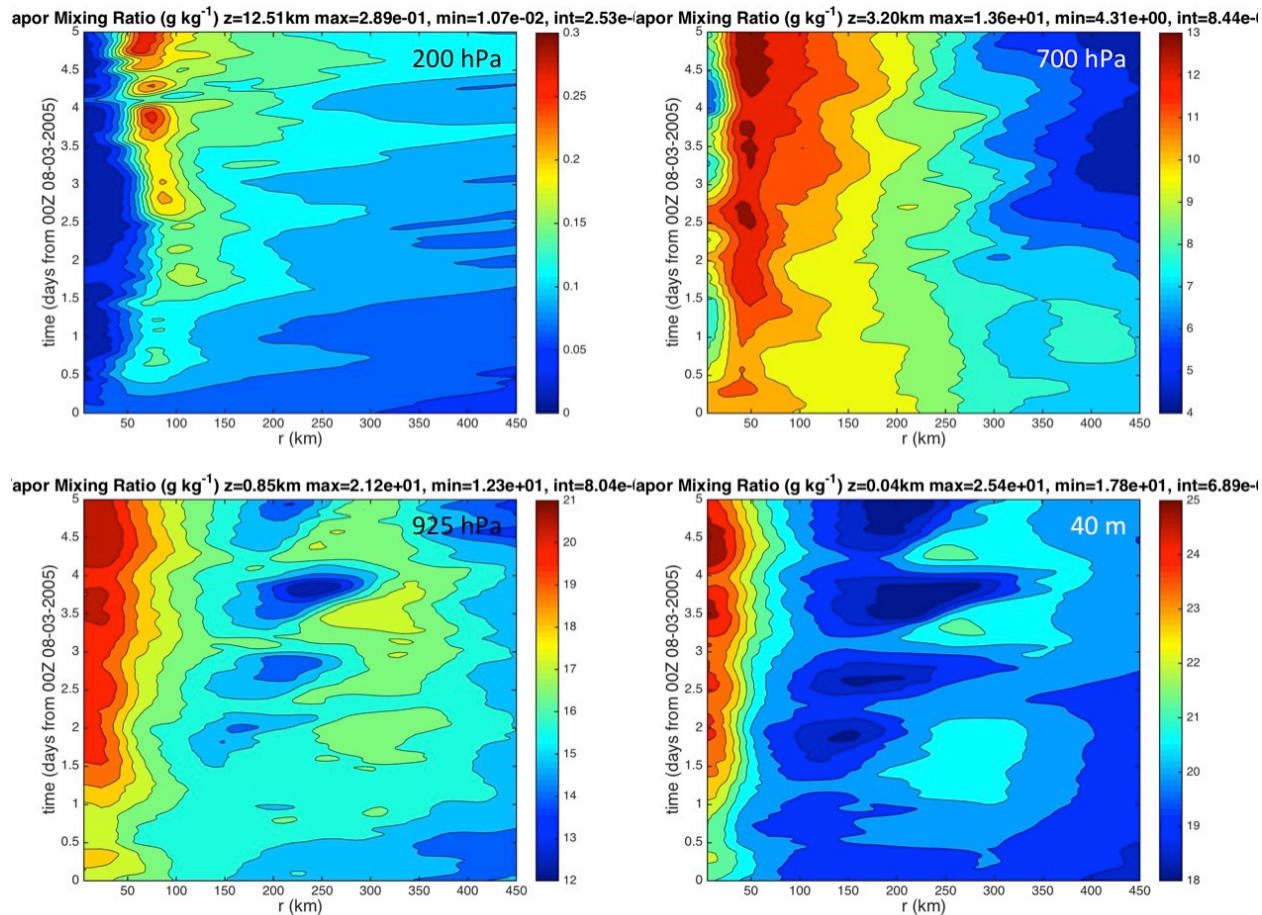


Figure 11: Hovmollers of azimuthally averaged mixing ratio ( $\text{g kg}^{-1}$ ) derived from the 03-08 August NRH1 study period for 200 hPa, 700 hPa, 925 hPa, and 40 m. Radii are analyzed relative to the TC center and extend out to 450 km.

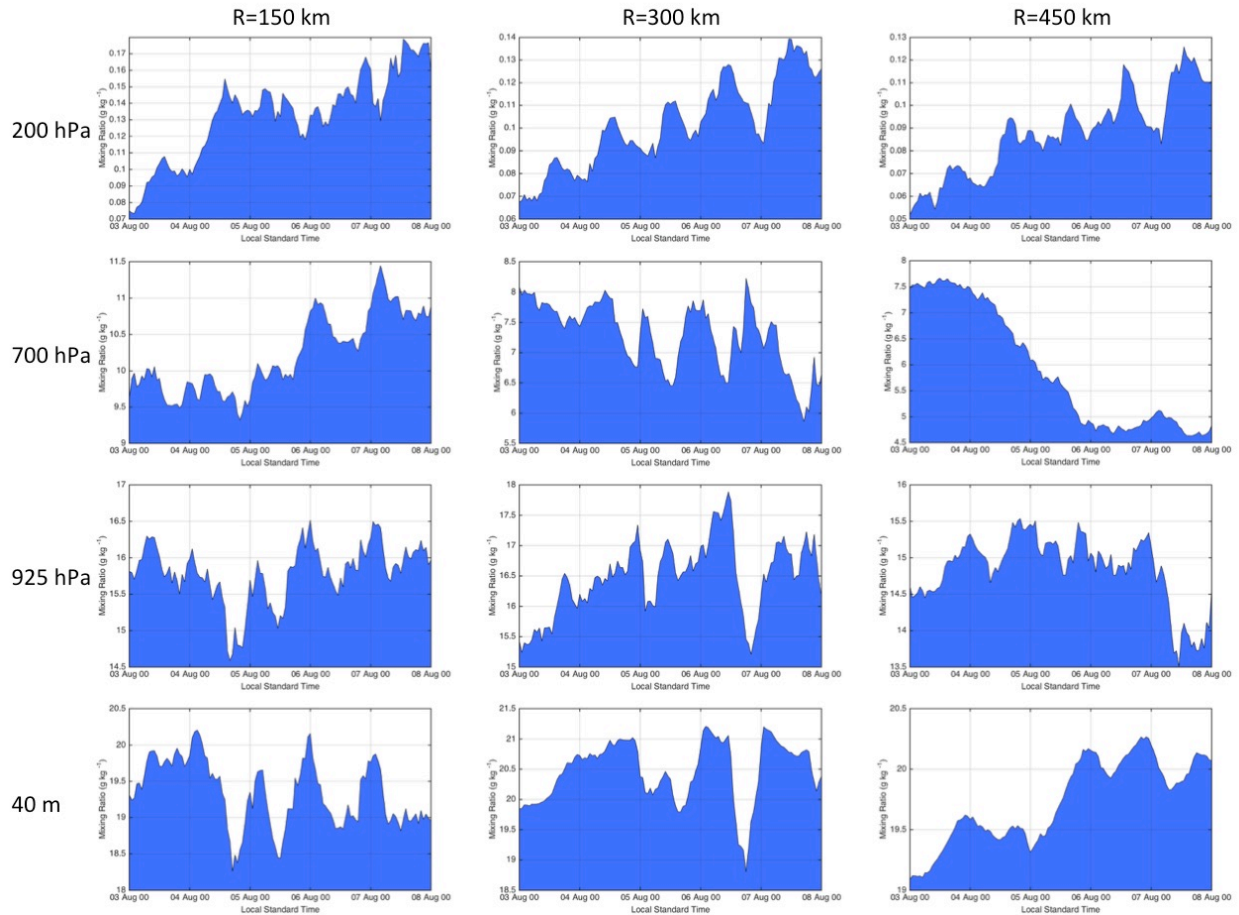


Figure 12: Azimuthally averaged mixing ratio ( $\text{g kg}^{-1}$ ) derived from the 03-08 August NRH1 study period for the 200 hPa, 700 hPa, 925 hPa, and 40 m vertical levels. Analyses include the 150, 300, and 450 km radii.

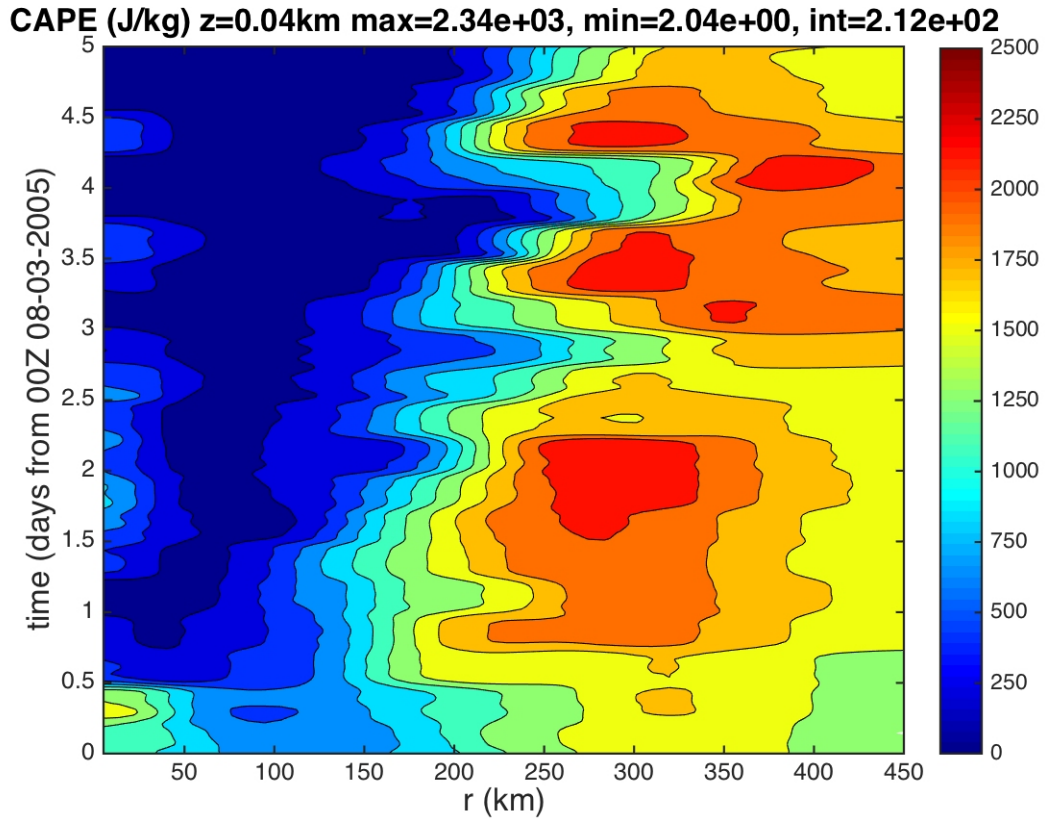


Figure 13: Hovmoller of azimuthally averaged CAPE ( $\text{J kg}^{-1}$ ) derived from the 03-08 August NRH1 study period. Radii are analyzed relative to the TC center and extend out to  $R=450$  km.

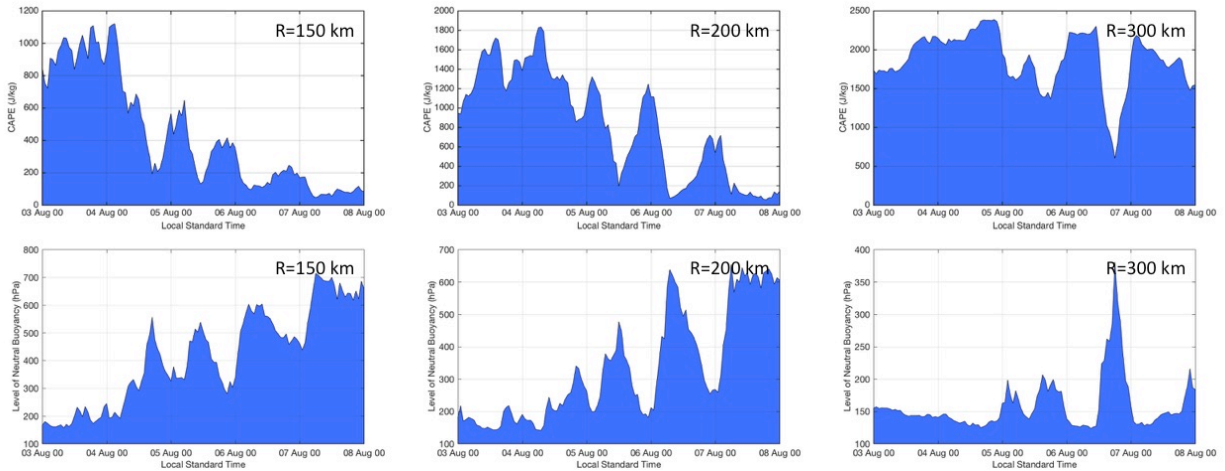


Figure 14: Azimuthally averaged CAPE (top) and the level of neutral buoyancy (LNB) derived from the 03-08 August NRH1 study period at the 150, 200, and 300 km radii.

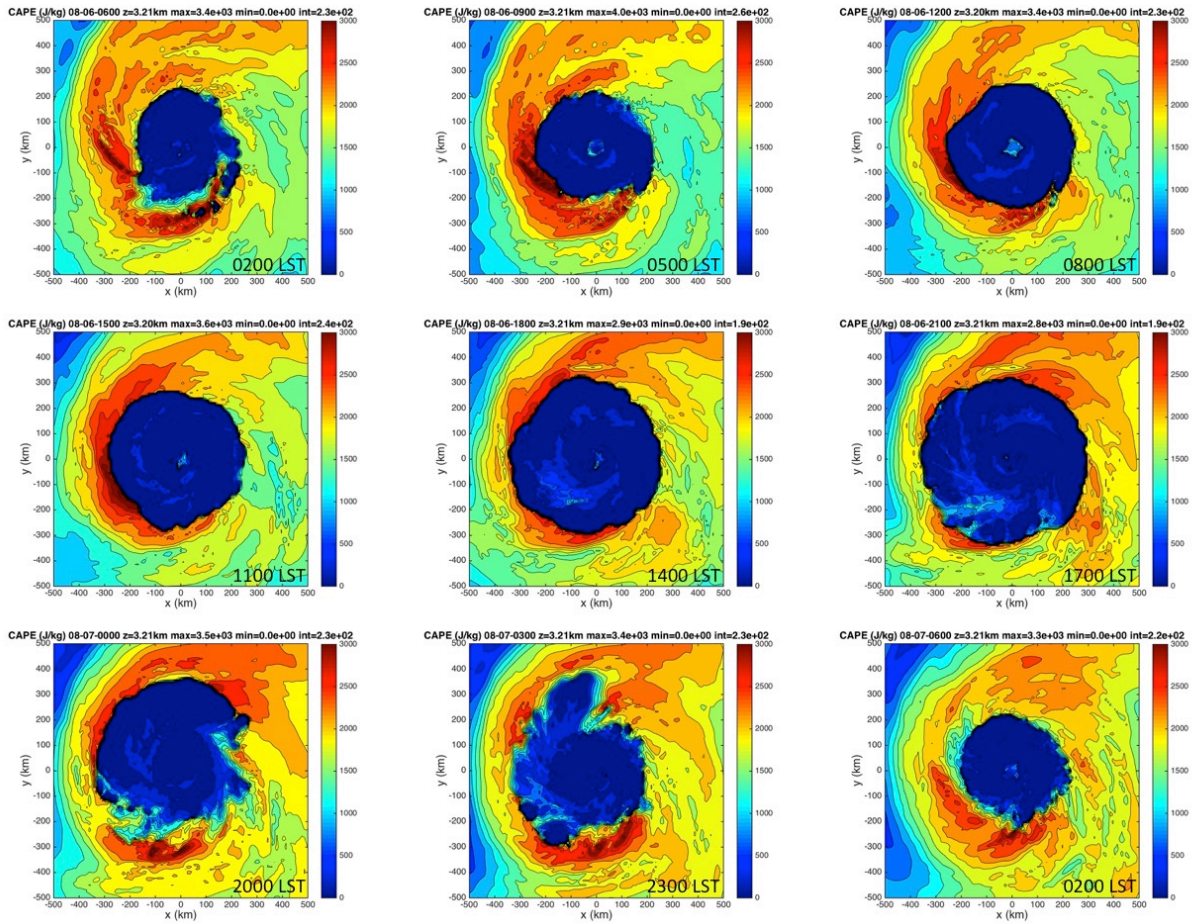


Figure 15: CAPE ( $\text{J kg}^{-1}$ ) derived from the NRH1 for 06-07 August. Images are 3-hourly from 06 Aug 0200 LST (0600 UTC) to 07 Aug 0200 LST (0600 UTC).

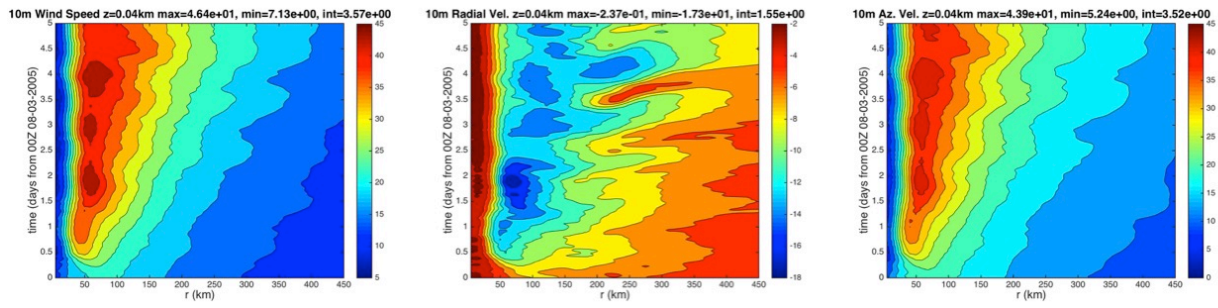


Figure 16: Hovmollers of azimuthally averaged 10-m surface winds ( $\text{m s}^{-1}$ ) derived from the 03-08 August NRH1 study period for (a) wind speed, (b) radial wind speed, and (c) tangential wind speed. Radii are analyzed relative to the TC center and extend out to  $R=450$  km.

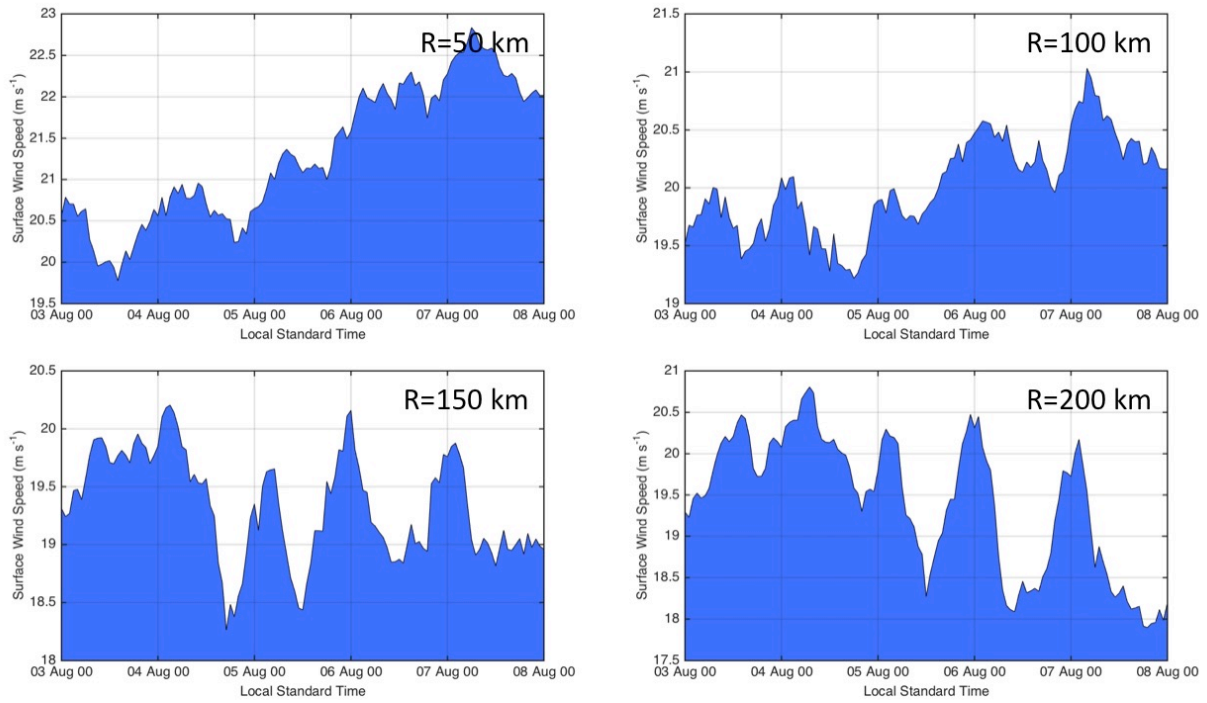


Figure 17: Plots of azimuthally averaged 10-m surface winds ( $\text{m s}^{-1}$ ) derived from the 03-08 August NRH1 study period for 50, 100, 150, and 200 km radii.

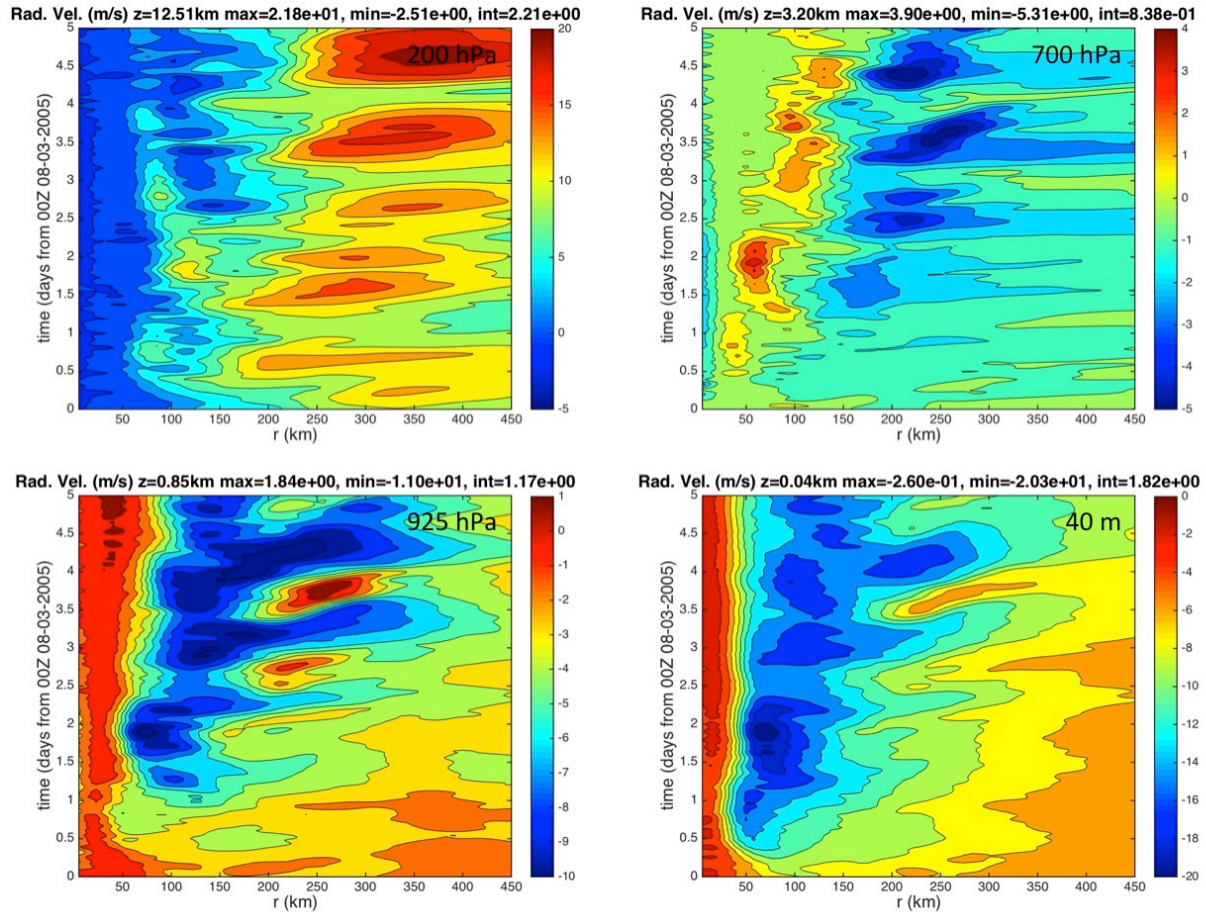


Figure 18: Hovmollers of azimuthally averaged radial wind ( $\text{m s}^{-1}$ ) derived from the 03-08 August NRH1 study period for 200 hPa, 700 hPa, 925 hPa, and 40 m. Radii are analyzed relative to the TC center and extend out to 450 km.

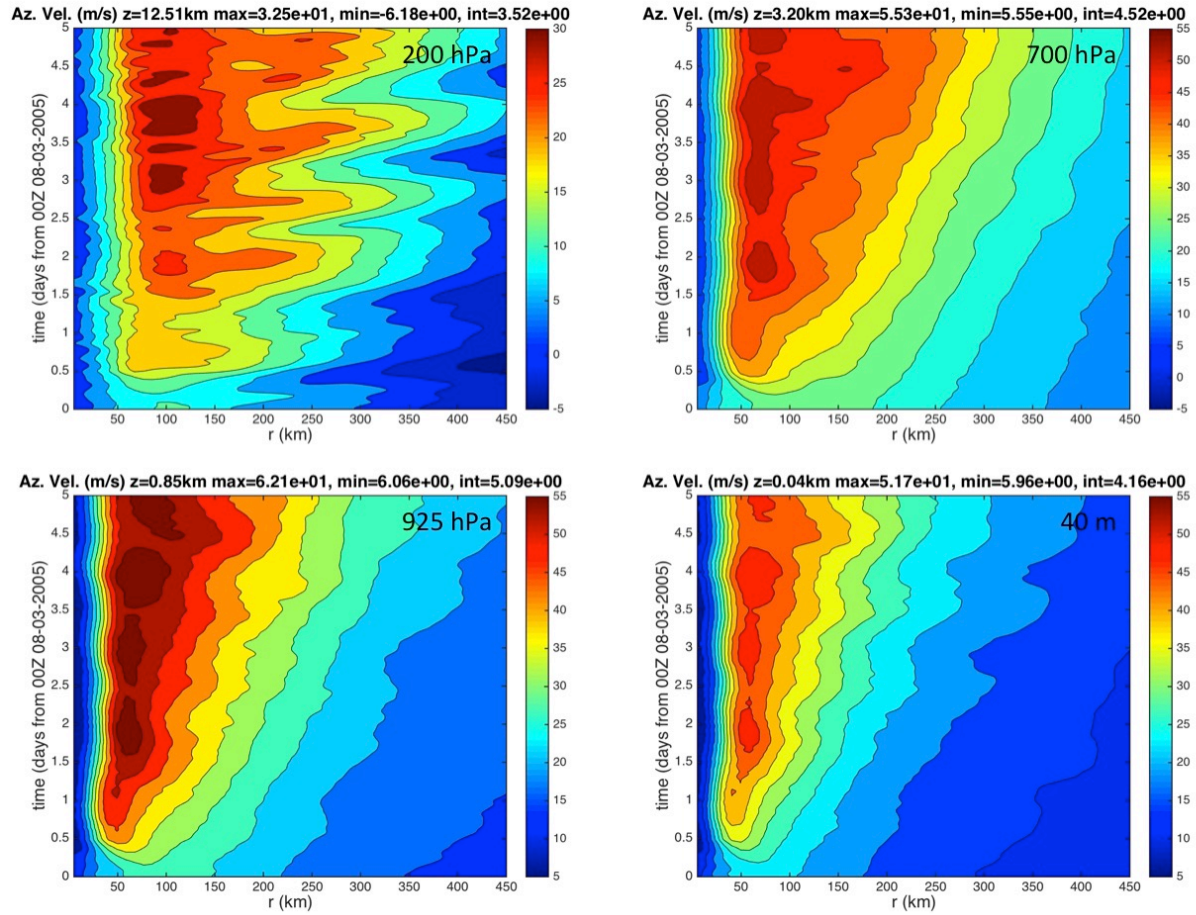


Figure 19: Hovmollers of azimuthally averaged tangential wind ( $\text{m s}^{-1}$ ) derived from the 03-08 August NRH1 study period for 200 hPa, 700 hPa, 925 hPa, and 40 m. Radii are analyzed relative to the TC center and extend out to  $R=450$  km.

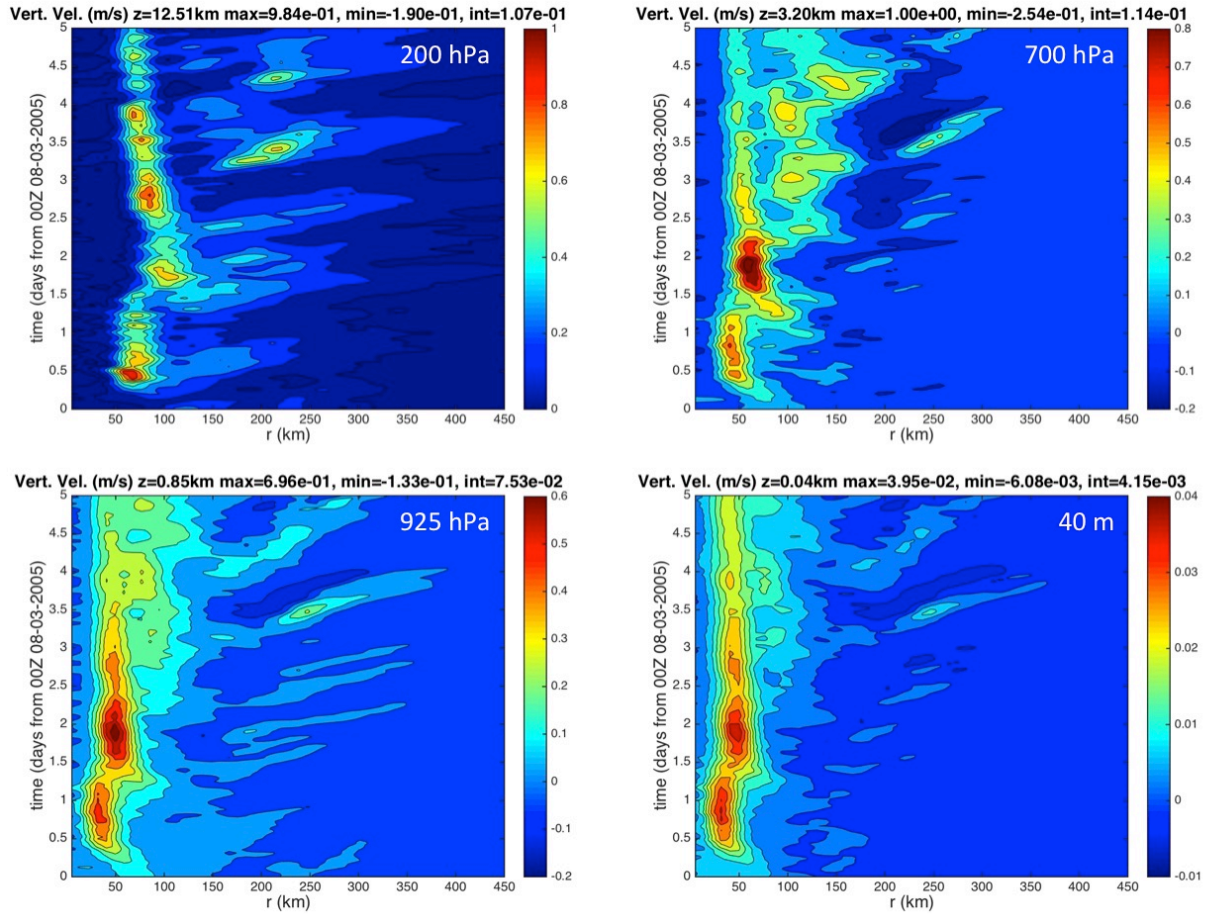


Figure 20: Hovmollers of azimuthally averaged vertical wind ( $\text{m s}^{-1}$ ) derived from the 03-08 August NRH1 study period for 200 hPa, 700 hPa, 925 hPa, and 40 m. Radii are analyzed relative to the TC center and extend out to 450 km.

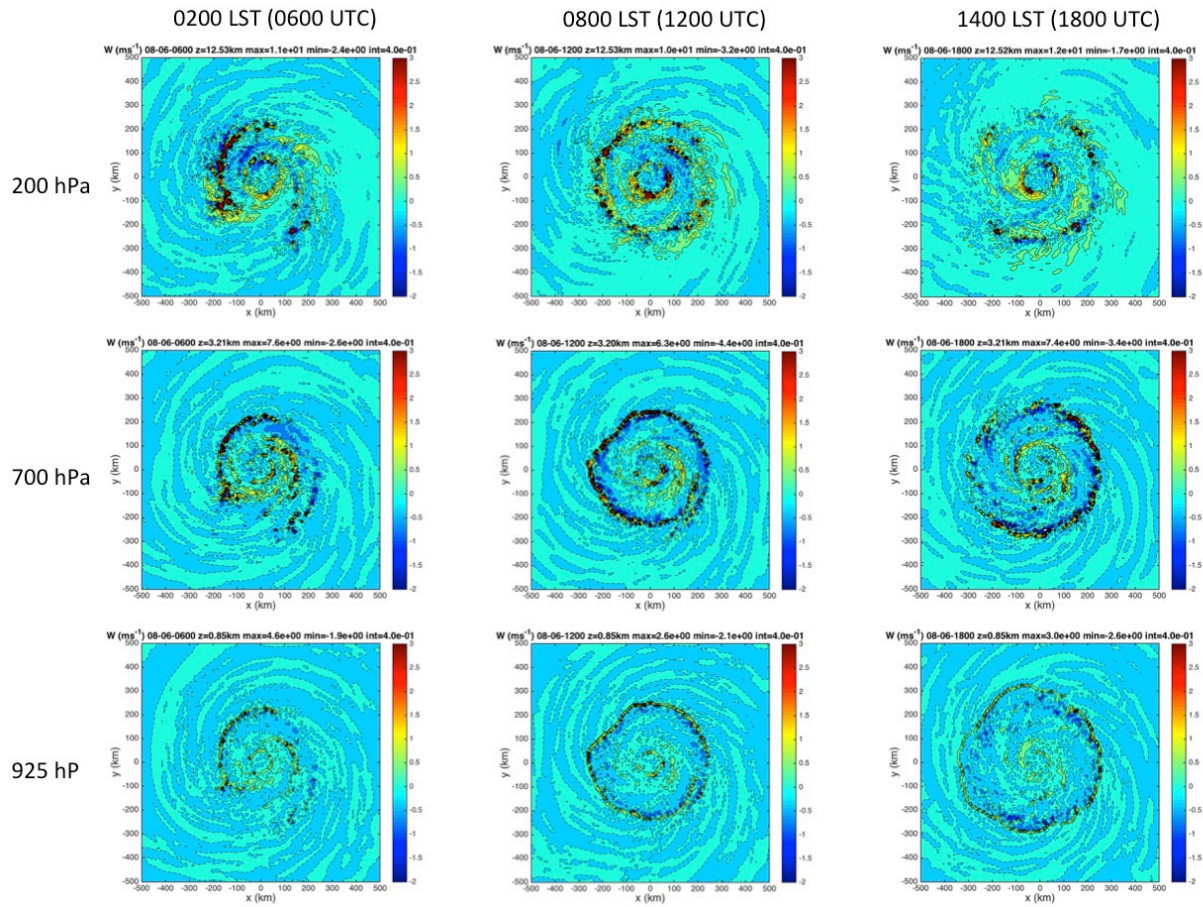


Figure 21: Plots of vertical wind ( $\text{m s}^{-1}$ ) derived from the NRH1 from 0200-1400 LST (0600-1800 UTC) on 06 August at 200 hPa, 700, and 925 hPa. A relatively deep layer semi-circular feature is indicated 200-300 km outside of the eyewall that has 1-3  $\text{m s}^{-1}$  vertical motion and is propagating away from the TC.

Rain Rate (mm/hr) z=12.51km max=5.18e+00, min=2.80e-04, int=4.71e-01

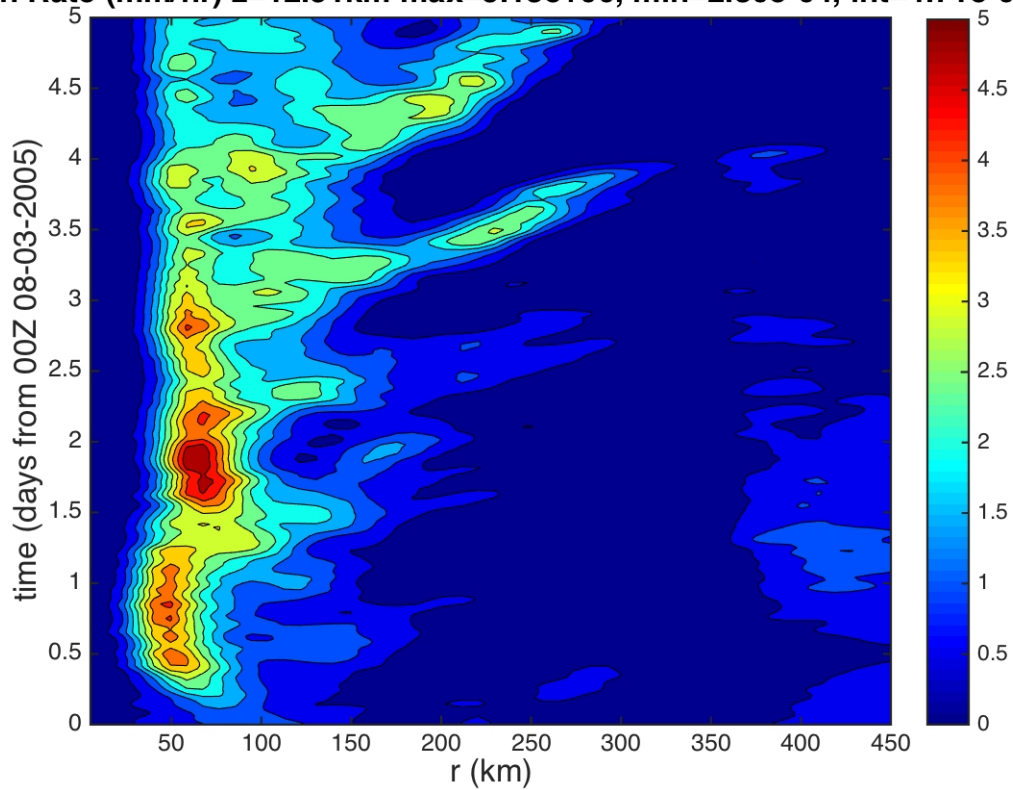


Figure 22: Hovmoller of rain rate ( $\text{mm h}^{-1}$ ) derived from the 03-08 August NRH1 study period. Radius is analyzed relative to the TC center and extends out to  $R=450$  km.

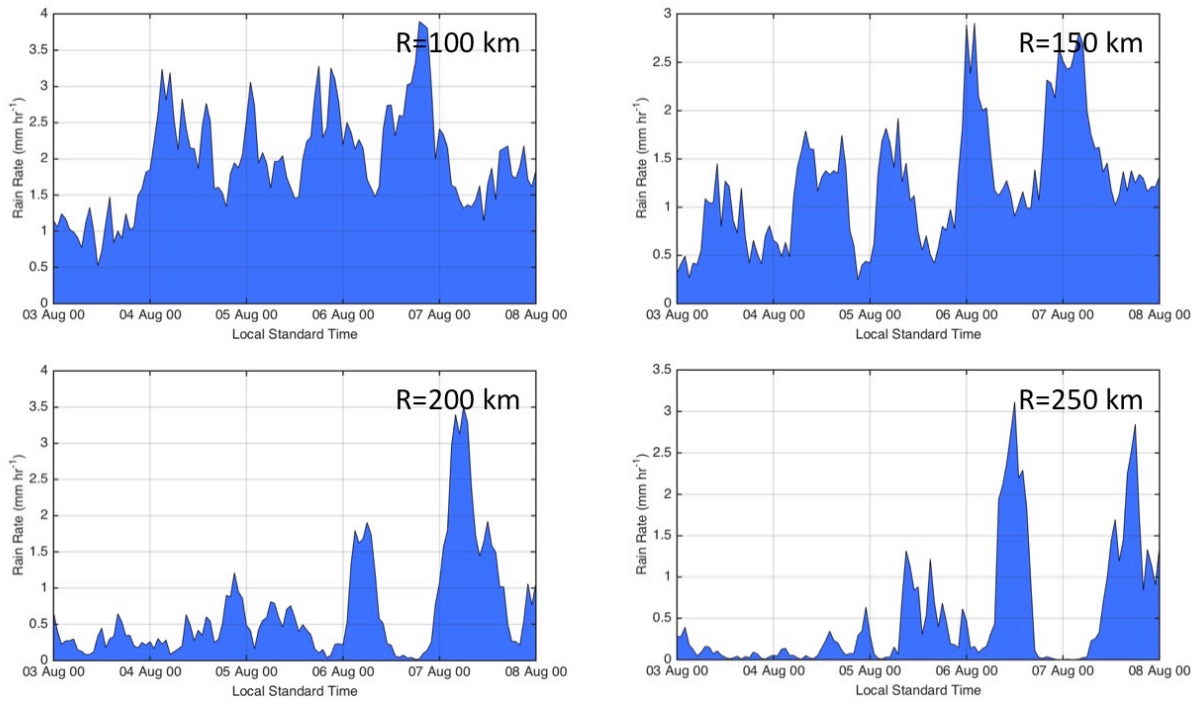


Figure 23: Plots of azimuthally averaged rain rate ( $\text{mm hr}^{-1}$ ) derived from the 03-08 August NRH1 study period at the 100, 150, 200, and 250 km radii.

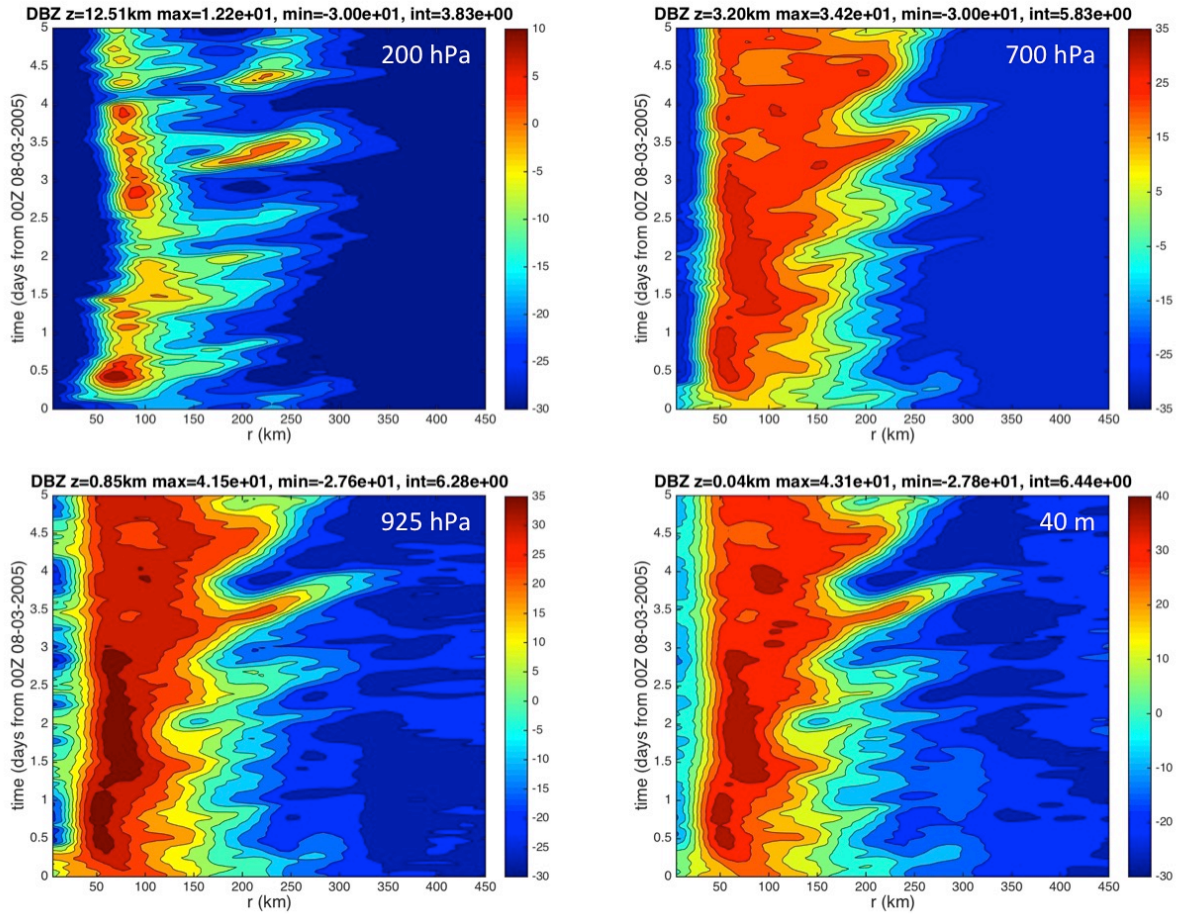


Figure 24: Hovmollers of simulated radar reflectivity (dBZ) derived from the 03-08 August NRH1 study period for 200 hPa, 700 hPa, 925 hPa, and 40 m. Radii are analyzed relative to the TC center and extend out to R=450 km.

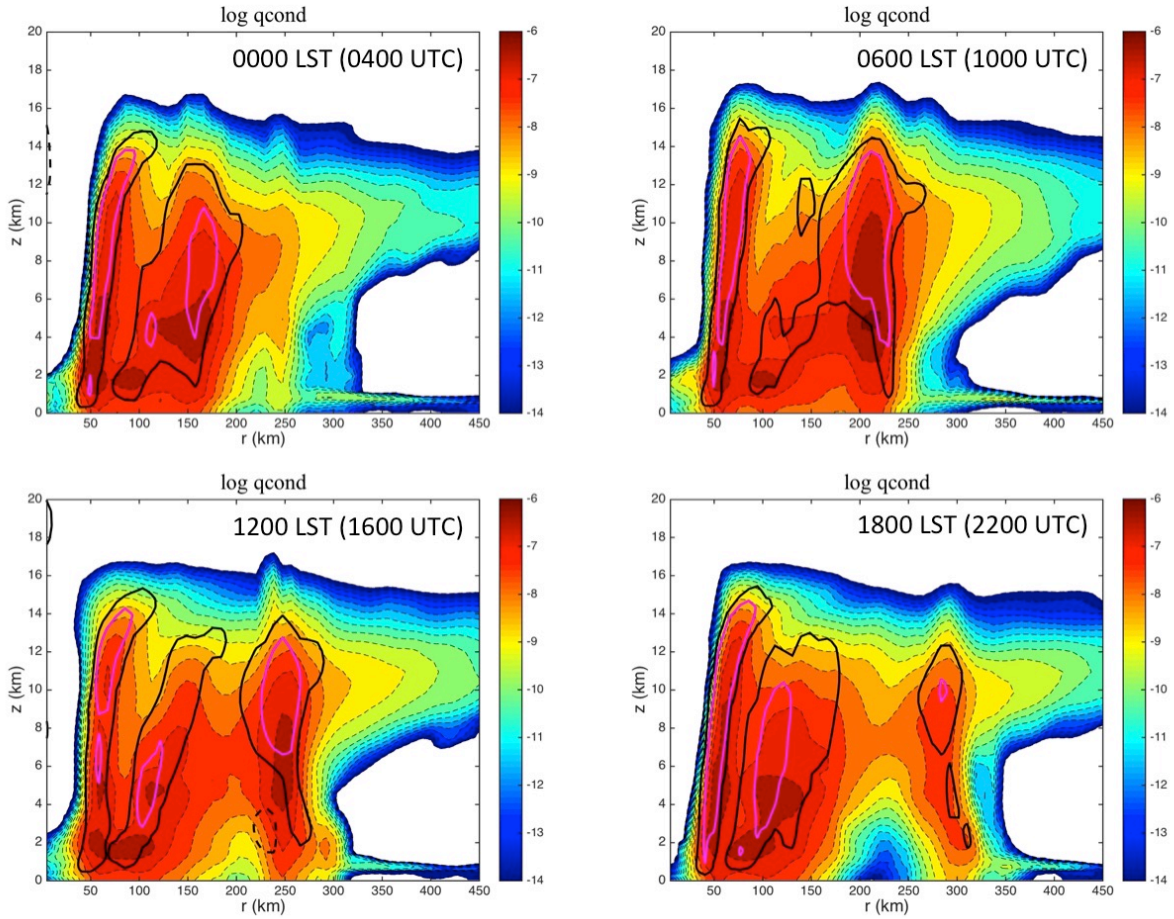


Figure 25: 6-hourly radius-height plots of Q-condensate from the NRH1 on 06 August from 0000-1800 LST (0400-2200 UTC). Dashed black, solid black, and magenta contours indicate azimuthal mean vertical winds of  $-0.25 \text{ ms}^{-1}$ ,  $+0.25 \text{ ms}^{-1}$ , and  $+0.5 \text{ ms}^{-1}$  respectively.

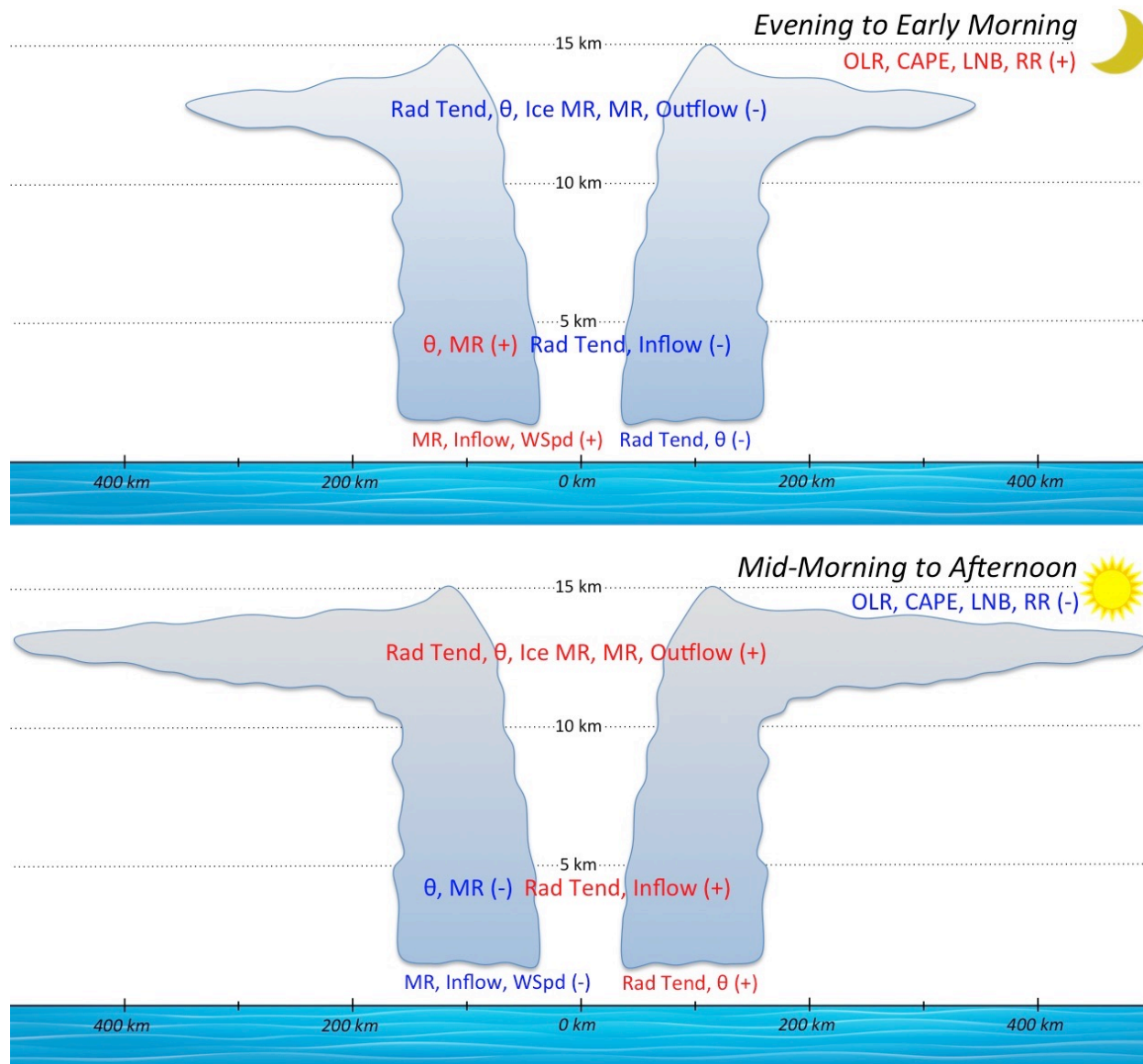


Figure 26: Schematic showing a TC in the (top) initial (i.e. nighttime) and (bottom) later (i.e. daytime) stages of the TCDC. The cross sections show background state parameters of total radiation tendency (Rad Tend,  $\text{K hr}^{-1}$ ),  $\theta$  (K), ice mixing ratio (Ice MR,  $\text{g kg}^{-1}$ ),  $V_r$ -indicated inflow/outflow (inflow/outflow,  $\text{m s}^{-1}$ ), and surface wind speed (WSpd,  $\text{m s}^{-1}$ ) at different levels of the storm. Single level/layer values of OLR ( $\text{W m}^{-2}$ ), CAPE ( $\text{J kg}^{-1}$ ), LNB (height), and rain rate ( $\text{mm h}^{-1}$ ) are labeled at the top right of each plot. Red (blue) lettering indicates diurnal maxima (minima) of the various parameters.

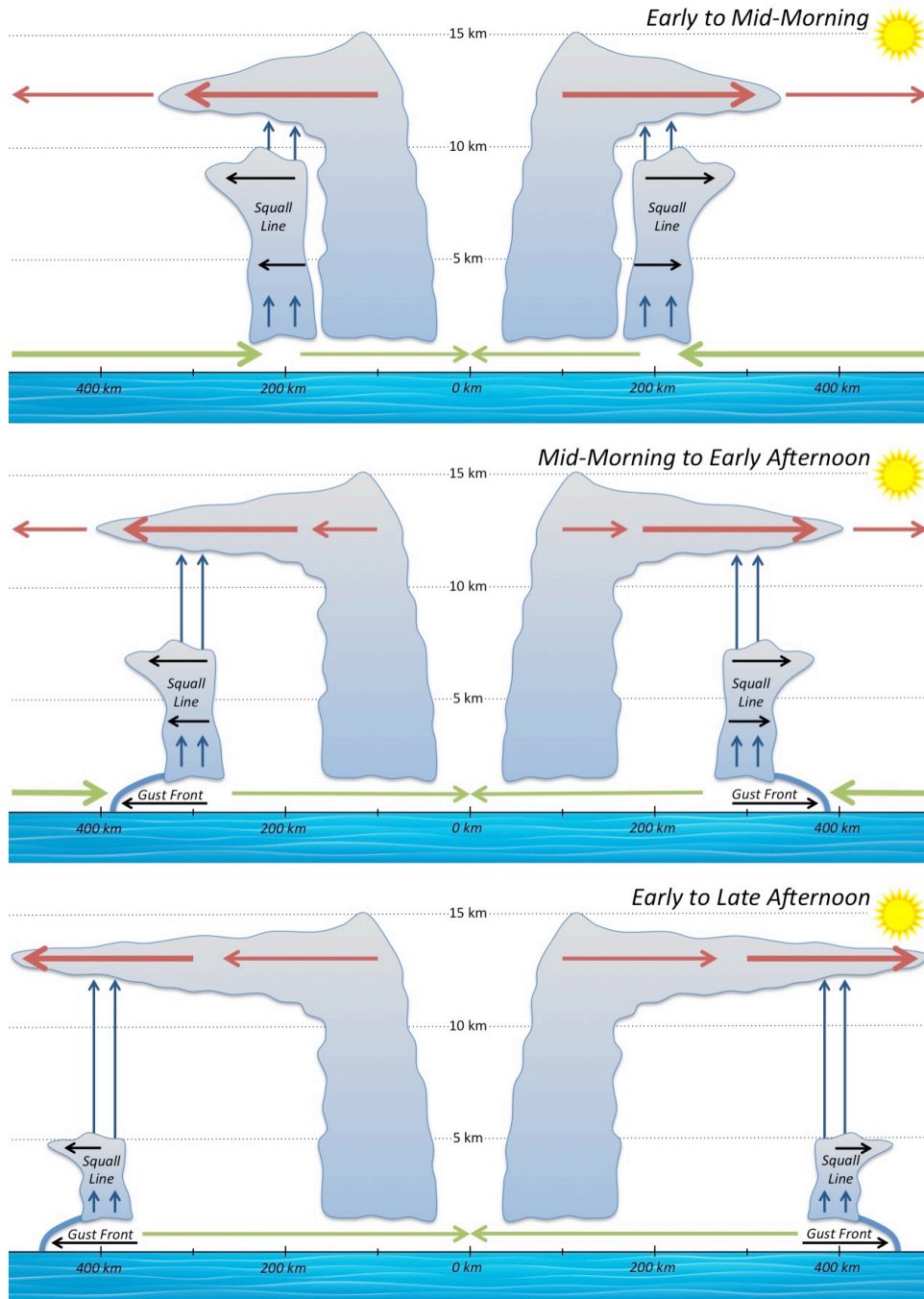


Figure 27: Schematic showing the evolution of a radially propagating TC diurnal pulse from the early morning to late afternoon. Upper level radial outflow (red arrows), lower level radial inflow (green arrows), and enhanced vertical wind at the location of the TC diurnal pulse (i.e. squall line, blue arrows) are shown. Gust fronts favored to form along the leading edge of the squall line beginning in the mid-morning to late afternoon when it is located at  $R \sim 300\text{--}400$  km are shown. Thickness of the radial outflow and inflow lines indicate relative strength at different times of day relative to the position of the squall line. The depth of the squall line is also suggested to lessen as it propagates away from the storm due to a lowering LNB that reaches a minimum in the afternoon.